Supporting Information

Electrochemical reduction conditioning modified Fe-based catalysts with structural disorders for efficient ammonium production from nitrite reduction

Maggie Lim,[a] Zhipeng Ma,[a] Denny Gunawan,[a] Ying Ying Ch'ng,[a] Wenyu Zhong,[a] Putri Ramadhany,[a] Karan Menon,[a] Daqian Ruan,[a] Priyank Kumar,[a] Ali R. Jalili,[b] Rose Amal,[a] Rahman Daiyan,*[c] Emma C Lovell*[a]

[a] Particles and Catalysis Research Laboratories and School of Chemical Engineering, UNSW Sydney, Sydney, NSW 2052, Australia

[b] School of Chemistry, UNSW Sydney, Sydney, NSW 2052, Australia

[c] Particles and Catalysis Research Laboratories and School of Minerals and Energy Resources Engineering, UNSW Sydney, Sydney, NSW 2052, Australia

* Corresponding authors

e.lovell@unsw.edu.au

r.daiyan@unsw.edu.au

Supporting Figures

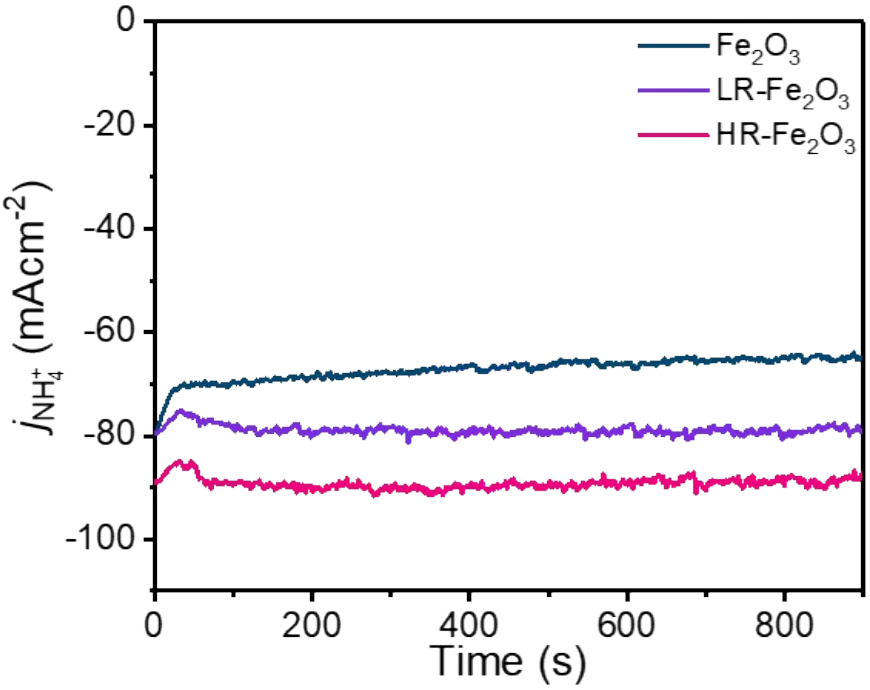

Figure S1. Chronoamperometric *i-t* curves of Fe_2O_3, LR-Fe_2O_3, and HR-Fe_2O_3 electrodes at NO_2RR applied potential of -1.0 V vs RHE. HR-Fe_2O_3 maintains the highest partial current density for NH_4^+ production of ~ 90.3 mA cm^{-2} among all samples at NO_2RR applied potential of -1.0 V vs RHE, followed by LR-Fe_2O_3 (~ 80 mA cm^{-2}), and lastly, pristine Fe_2O_3 (~ 66 mA cm^{-2}).

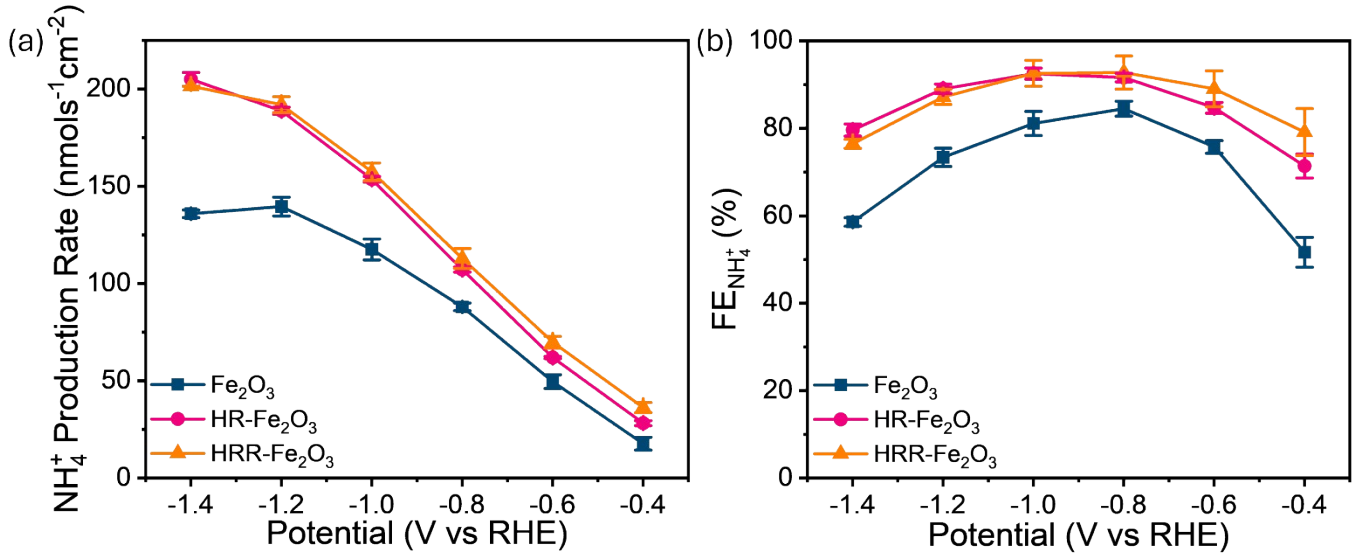

Figure S2. NO_2RR-to-NH_4^+ production performances of Fe_2O_3, HR-Fe_2O_3, and HRR-Fe_2O_3 electrodes across an applied potential range of -1.4 to -0.4 V vs RHE: **(a)** NH_4^+ production rate and **(b)** Faradaic efficiency (FE_{NH4+}). The HRR-Fe_2O_3 catalyst exhibits essentially identical performance to the HR-Fe_2O_3 electrode, showing overlapping trends in both NH_4^+ production rate and FE_{NH4+} across the applied potentials from -0.4 to 1.4 V vs RHE, with only minor differences within experimental error.

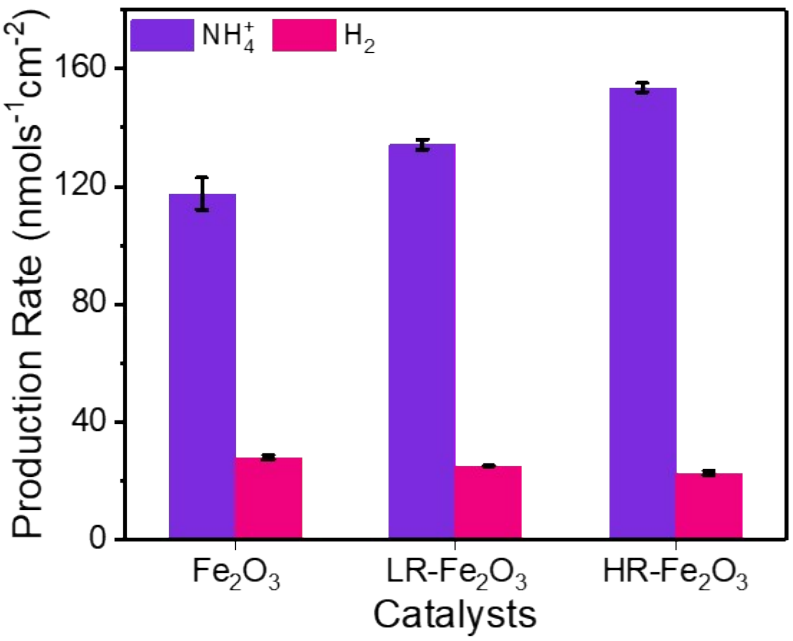

Figure S3. Comparison of NH_4^+ and H_2 production rates of Fe_2O_3, LR-Fe_2O_3, and HR-Fe_2O_3 electrodes at NO_2RR applied potential of -1.0 V vs RHE. HR-Fe_2O_3 generates the least amount of H_2 (22 nmol s^{-1} cm^{-2}), followed by LR-Fe_2O_3 (25 nmol s^{-1} cm^{-2}), with pristine Fe_2O_3 producing the most (28 nmol s^{-1} cm^{-2}).

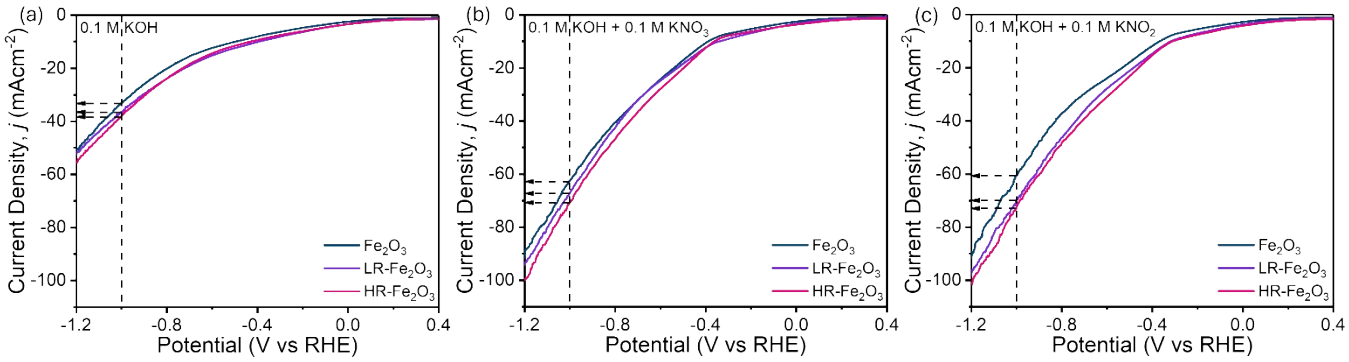

Figure S4. Polarization curves of Fe_2O_3, LR-Fe_2O_3, and HR-Fe_2O_3 electrodes at scan rate of 5 mV s^{-1} in electrolyte condition of **(a)** 0.1 M KOH, **(b)** 0.1 M KOH + 0.1 M KNO_3, and **(c)** 0.1 M KOH + 0.1 M KNO_2. These polarization curves indicate that both LR-Fe_2O_3 and HR-Fe_2O_3 exhibit slight improvements in total current densities (*j*) compared to pristine Fe_2O_3 across tested potentials in all types of electrolytes. For instance, at -1.0 V vs RHE in 0.1 M KOH + 0.1 M KNO_2 electrolyte, the *j* achieved by pristine Fe_2O_3 is -60.1 mA cm^{-2}, while LR-Fe_2O_3 and HR-Fe_2O_3 show improvements of ~ 16% (-69.9 mA cm^{-2}) and ~ 22% (-73.0 mA cm^{-2}), respectively. Similarly, in the electrolytes of 0.1 M KOH only and 0.1 M KOH + 0.1 M KNO_3, at -1.0 V vs RHE, HR-Fe_2O_3 achieves the highest *j* of ~ -38.2 and -70.7 mA cm^{-2}, representing improvements of ~ 15% and 13% over pristine Fe_2O_3 (-33.1 and -62.8 mA cm^{-2}, respectively). LR-Fe_2O_3 shows modest improvements of ~ 10% (~ -36.4 mA cm^{-2}) and ~ 6.8% (-67.1 mA cm^{-2}) in the same electrolytes. These results suggest that post-conditioned Fe_2O_3 catalysts exhibit slightly enhanced intrinsic activity overall.

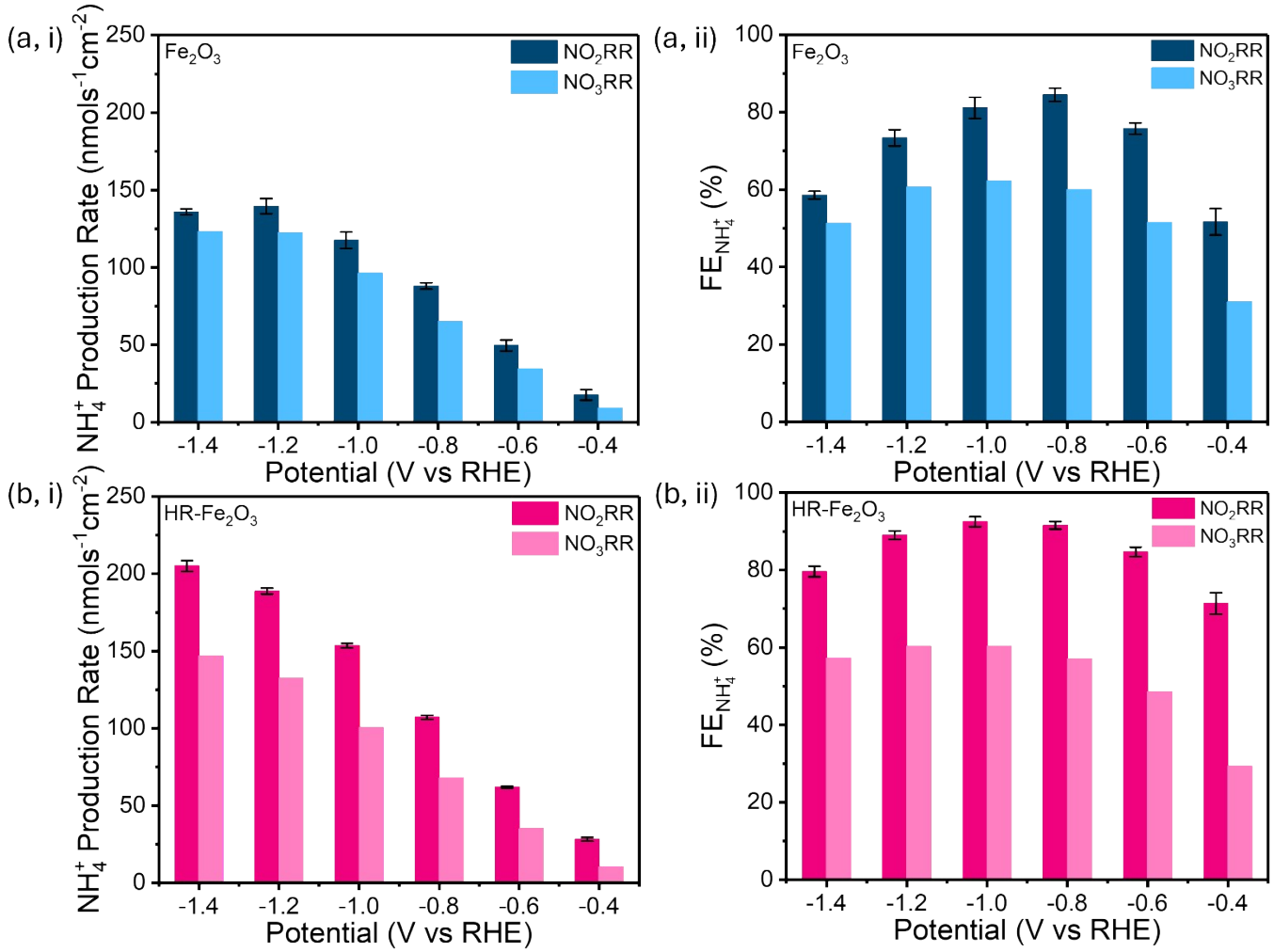

Figure S5. Performance comparison between NO_2RR and NO_3RR activity of **(a)** pristine Fe_2O_3 and **(b)** HR-Fe_2O_3 electrodes across an applied potential range of -1.4 to -0.4 V vs RHE: **(i)** NH_4^+ production rate and **(ii)** Faradaic efficiency (FE_{NH4+}). The results clearly demonstrate that both electrodes produce greater NH_4^+ and FE_{NH4+} in NO_2RR than in NO_3RR, with HR-Fe_2O_3 consistently outperforming pristine Fe_2O_3 in both reactions. Specifically, for NO_2RR, HR-Fe_2O_3 achieves a peak FE_{NH4+} of 93% at -1.0 V vs RHE, with an NH_4^+ production rate of ~ 154 nmol s^{-1} cm^{-2}. This represents a 31% improvement in productivity and 15% increase in FE_{NH4+} compared to pristine Fe_2O_3 (~ 118 nmol s^{-1} cm^{-2} and 81% at -1.0 V vs RHE). For NO_3RR, HR-Fe_2O_3 also outperforms pristine Fe_2O_3, achieving an NH_4^+ production rate of ~101 nmol s^{-1} cm^{-2} at -1.0 V vs RHE, corresponding to a 5% improvement over pristine Fe_2O_3 (~ 96 nmol s^{-1} cm^{-2}). However, for FE_{NH4+} in NO_3RR, both pristine Fe_2O_3 and HR-Fe_2O_3 exhibit nearly identical performance across the applied potentials. For example, at -1.0 V vs RHE, HR-Fe_2O_3 achieves a FE_{NH4+} of 61%, while pristine Fe_2O_3 achieves 62%. Importantly, the results indicate that the improvements in NH_4^+ production are more pronounced in NO_2RR than in NO_3RR following the electroreduction conditioning (ERC) treatment. This suggests that the ERC-treated Fe_2O_3 catalysts are more surface-active for NO_2RR than NO_3RR, and that ERC treatment yields better performance enhancements in NO_2RR.

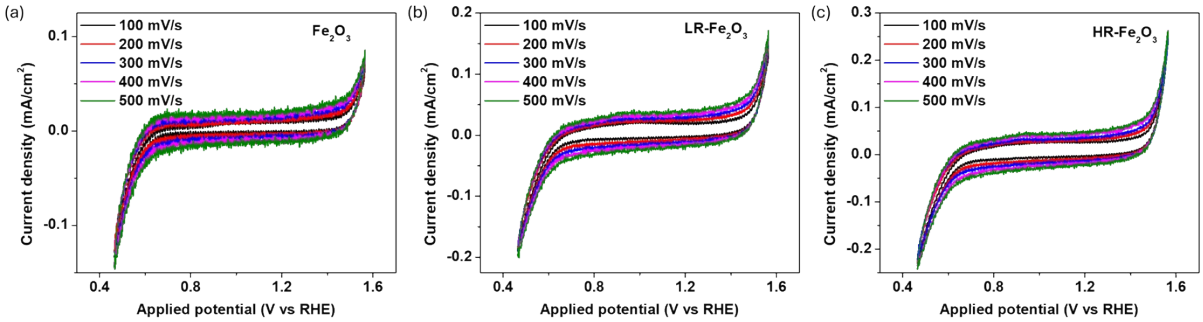

Figure S6. The cyclic voltammetry (CV) curves of Fe_2O_3, LR-Fe_2O_3, and HR-Fe_2O_3 electrodes collected under different scan rates of 100, 200, 300, 400, and 500 mV/s were used for ECSA calculations.

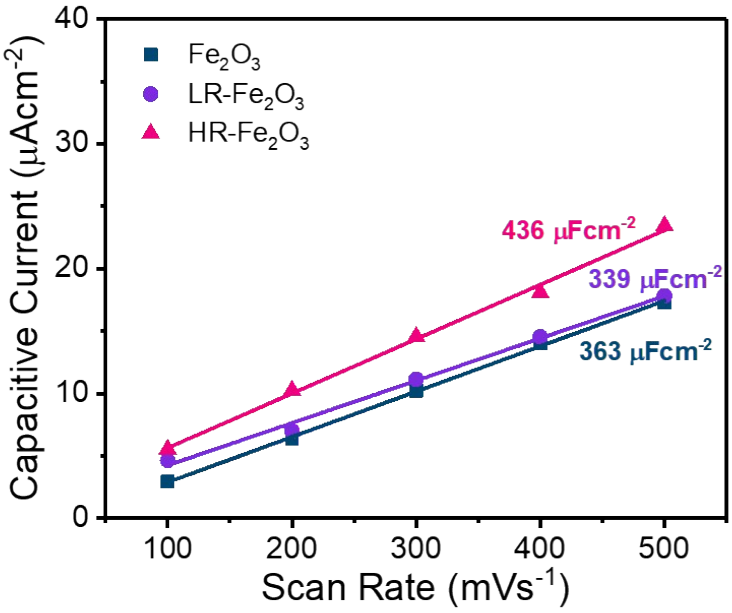

Figure S7. Double-layer capacitance (CDL) of Fe_2O_3, LR-Fe_2O_3, and HR-Fe_2O_3 electrodes, computed from cyclic voltammetry measurements. These specific capacitance values are used to compute ECSAs of the catalysts as presented in **Table S1**.

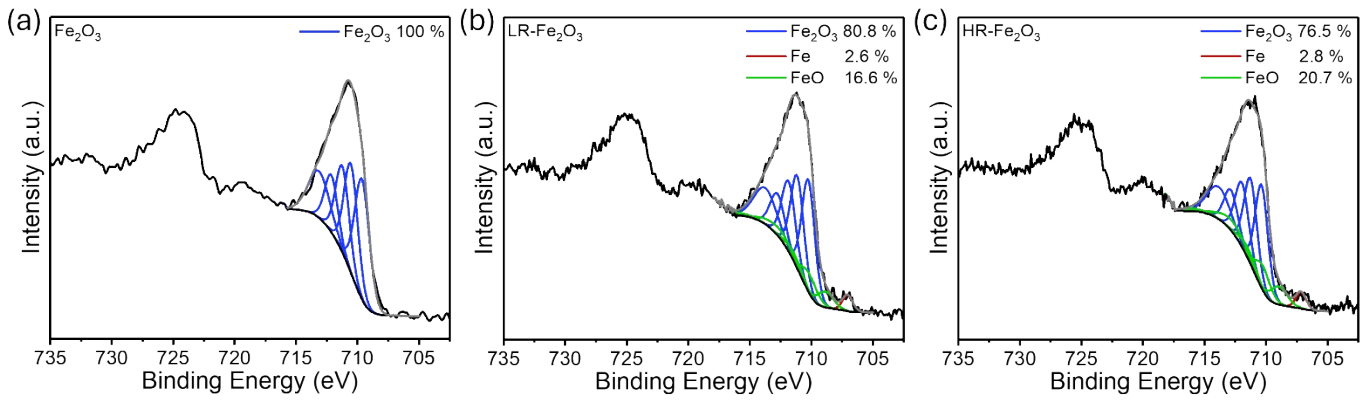

Figure S8. Curve fittings to the high-resolution X-ray photoelectron spectroscopy (XPS) Fe 2p spectra of **(a)** Fe_2O_3, **(b)** LR-Fe_2O_3 and **(c)** HR-Fe_2O_3. The results demonstrate that increasing the (more negative) ERC potential leads to further reduction of Fe species. Specifically, when the electrode is preconditioned at a low reduction (LR) potential (-1.0 V vs RHE), 19.2% of Fe_2O_3 in LR-Fe_2O_3 is reduced to Fe and FeO, accounting for 2.6% and 16.6%, respectively. At a more negative (high reduction, HR) treatment potential (-2.0 V vs RHE), HR-Fe_2O_3 experiences a slightly larger portion of Fe_2O_3 (23.5%) being reduced to Fe and FeO, comprising 2.8% and 20.7%, respectively. The emergence of these FeO and metallic Fe on the catalyst surface creates FeO/Fe/Fe_2O_3 interfaces, suggesting the construction of Fe oxide interfaces after ERC treatment.

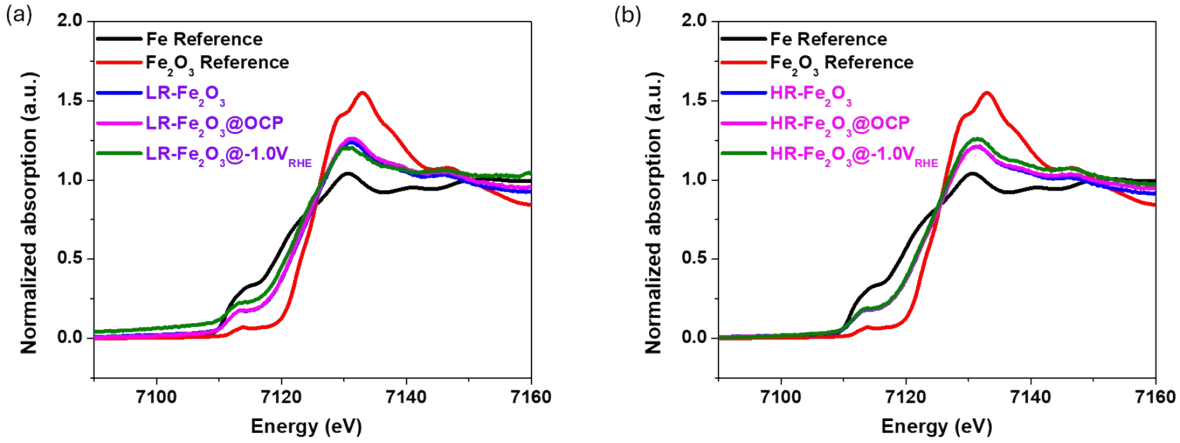

Figure S9. *Ex situ* XANES spectra and *in situ* XANES spectra of (a) LR-Fe_2O_3 and (b) HR-Fe_2O_3 catalysts collected under experimental conditions of open-circuit potential and -1.0 V vs RHE in 0.1 M KOH with 0.1 M KNO_2 electrolyte.

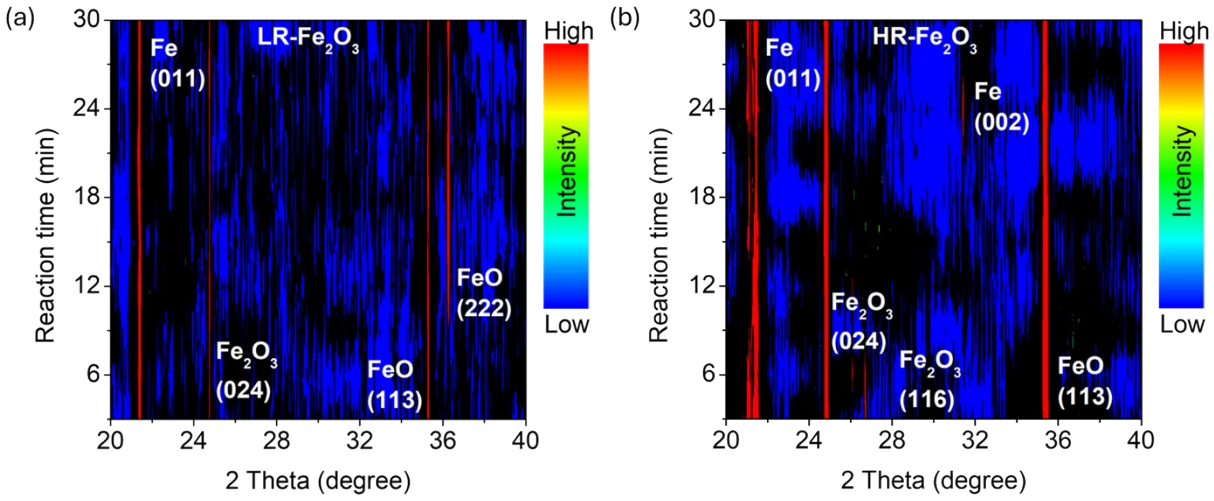

Figure S10. *In situ* powder diffraction (PD) of LR-Fe_2O_3 and HR-Fe_2O_3 catalysts at -1.0 V vs RHE in 0.1 M KOH with 0.1 M KNO_2 electrolyte for continuous tests of 30 minutes.

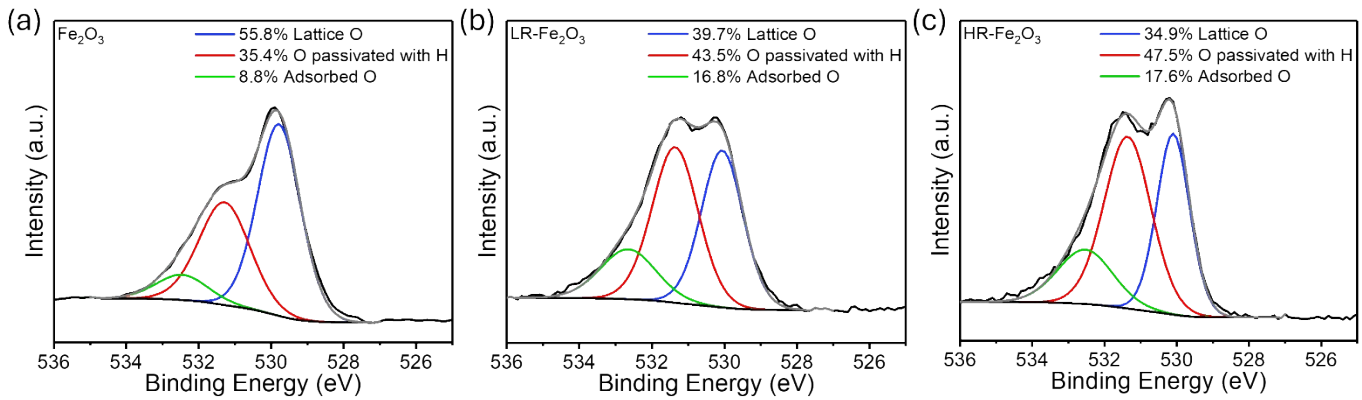

Figure S11. Curve fittings to the high-resolution XPS O 1s spectra of **(a)** Fe_2O_3, **(b)** LR-Fe_2O_3 and **(c)** HR-Fe_2O_3. The results show a clear decrease in the proportion of lattice oxygen (peak at ~ 530 eV)[1] after ERC, which is consistent with the reduction of Fe_2O_3 evidenced by Fe 2p XPS spectra. Specifically, LR-Fe_2O_3 consists of 39.7% lattice oxygen, while HR-Fe_2O_3 comprises 34.9%, both markedly lower than pristine Fe_2O_3 (55.8%). Two other peaks at ~ 531.0 and 532.5 eV are attributed to surface oxygen passivated with hydrogen and adsorbed oxygen (water), respectively.[2,3] The content of surface oxygen passivated with hydrogen increases from 35.4% in pristine Fe_2O_3 to 43.5% in LR-Fe_2O_3 and further to 47.5% in HR- Fe_2O_3 Similarly, adsorbed oxygen (water) increases from 8.8% in pristine Fe_2O_3 to 16.8% in LR-Fe_2O_3 and 17.6% in HR-Fe_2O_3.

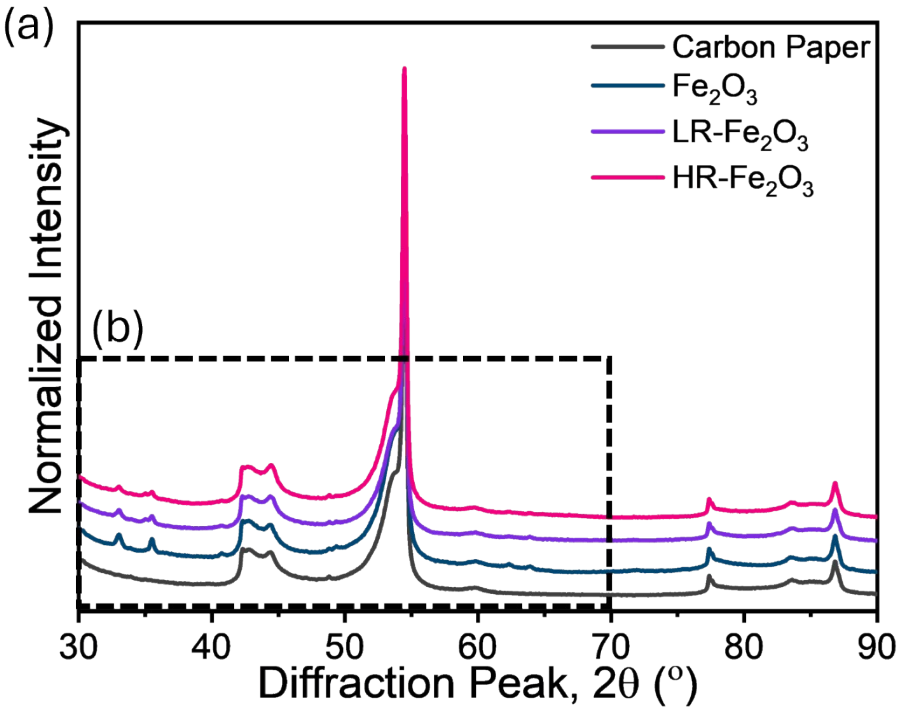

Figure S12. (a) Normalized X-ray diffraction (XRD) patterns (intensity normalized to the highest peak) of pristine Fe_2O_3, LR-Fe_2O_3, and HR-Fe_2O_3, with **(b)** excerpt for patterns in diffraction peak range of 30° to 70° as presented in **Figure 2b, i**. The XRD patterns show that pristine Fe_2O_3 displays peaks at ~ 33.0, 35.5, 40.7, 49.4, 62.3, and 63.9°, corresponding to the (104), (110), (113), (024), (214), and (300) planes of α-Fe_2O_3, respectively (JCPDS collection code: 01-080-0597). The post-conditioned electrodes, LR-Fe_2O_3 and HR-Fe_2O_3, exhibit similar peaks, confirming the retention of the α-Fe_2O_3 structure. However, a new split from the (110) peak at ~ 35.0°, is observed to appear in both conditioned samples. This split peak, corresponding to the (101) plane of α-Fe_2O_3, indicates a partial phase shift in the crystal structure. The diffraction features at 40-45° and 50-55° are attributed to the (100)/(101) and (004) planes of graphitic carbon, respectively, originating from the carbon paper substrate (ICDD:01-075-1621).

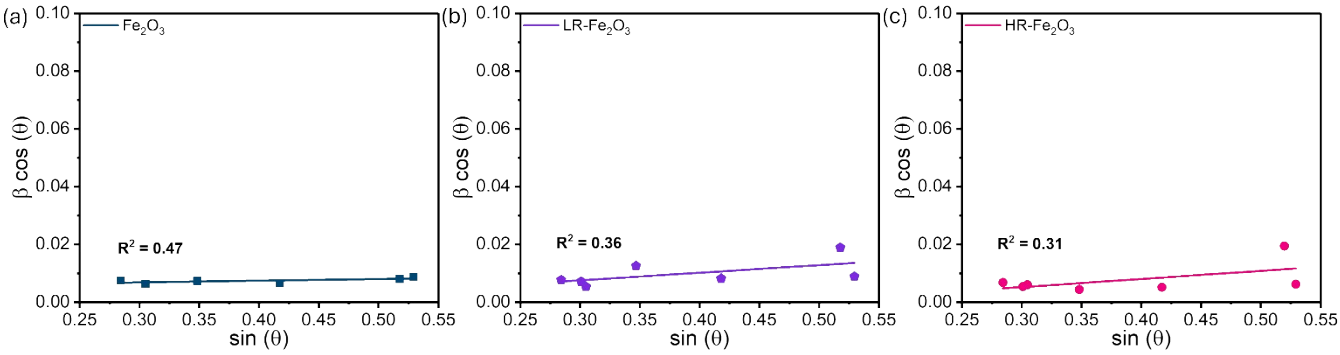

Figure S13. Williamson-Hall (WH) plots of **(a)** pristine Fe_2O_3, **(b)** LR-Fe_2O_3, and **(c)** HR-Fe_2O_3. The WH plots estimate lattice strains of 6.0%, 26.3%, and 28.0% for Fe_2O_3, LR-Fe_2O_3, and HR-Fe_2O_3, respectively.

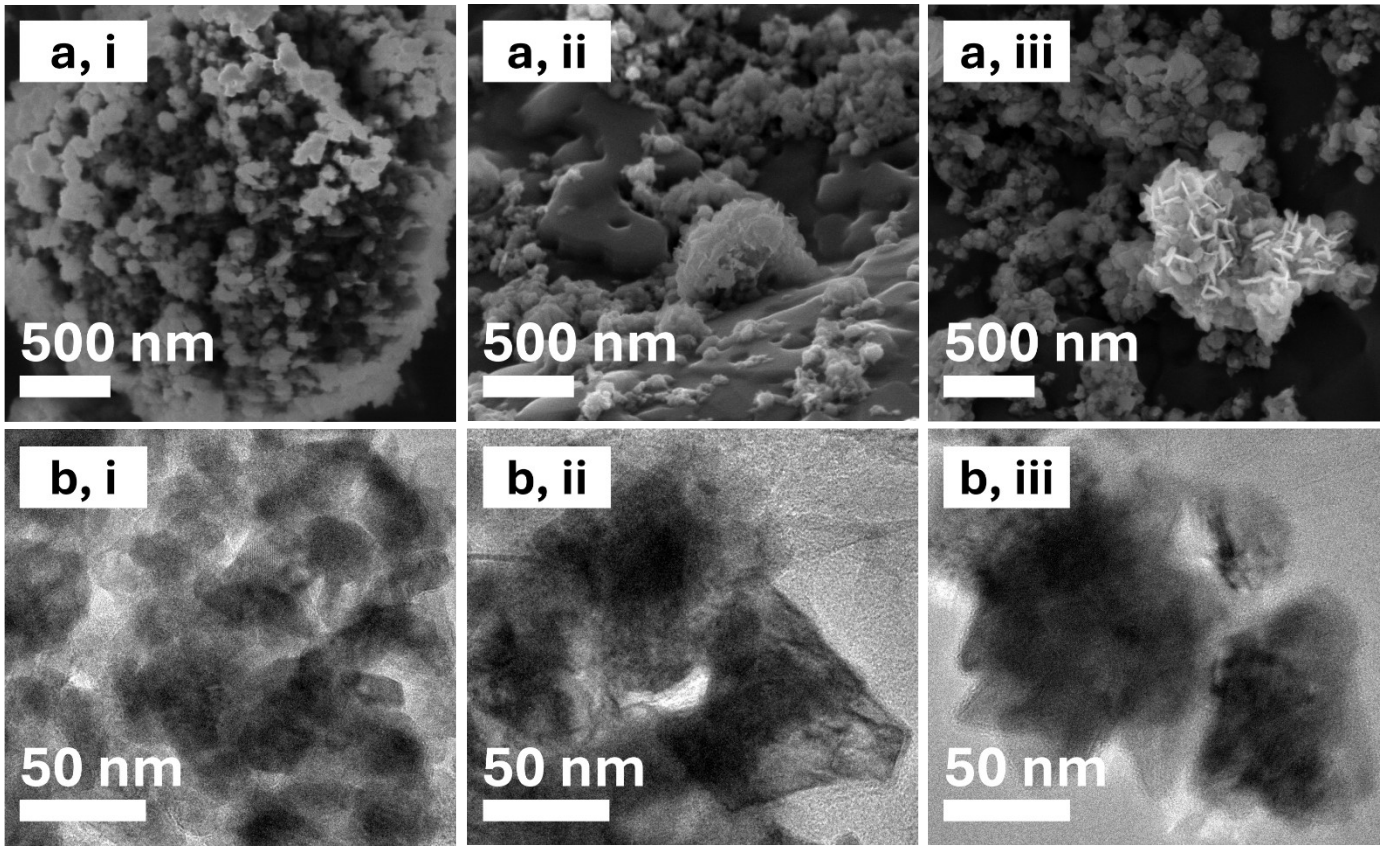

Figure S14. (a) Scanning electron microscopy **(**SEM) and **(b)** transmission electron microscopy (TEM) images of **(i)** pristine Fe_2O_3, **(ii)** LR- Fe_2O_3, and **(iii)** HR- Fe_2O_3. The pristine Fe_2O_3 catalyst displays morphology with irregular spherical nanoparticles that agglomerate into large clusters. After ERC, both LR-Fe_2O_3 and HR-Fe_2O_3 present a morphology consisting of a mixture of irregular spherical and plate-like shaped nanoparticles.

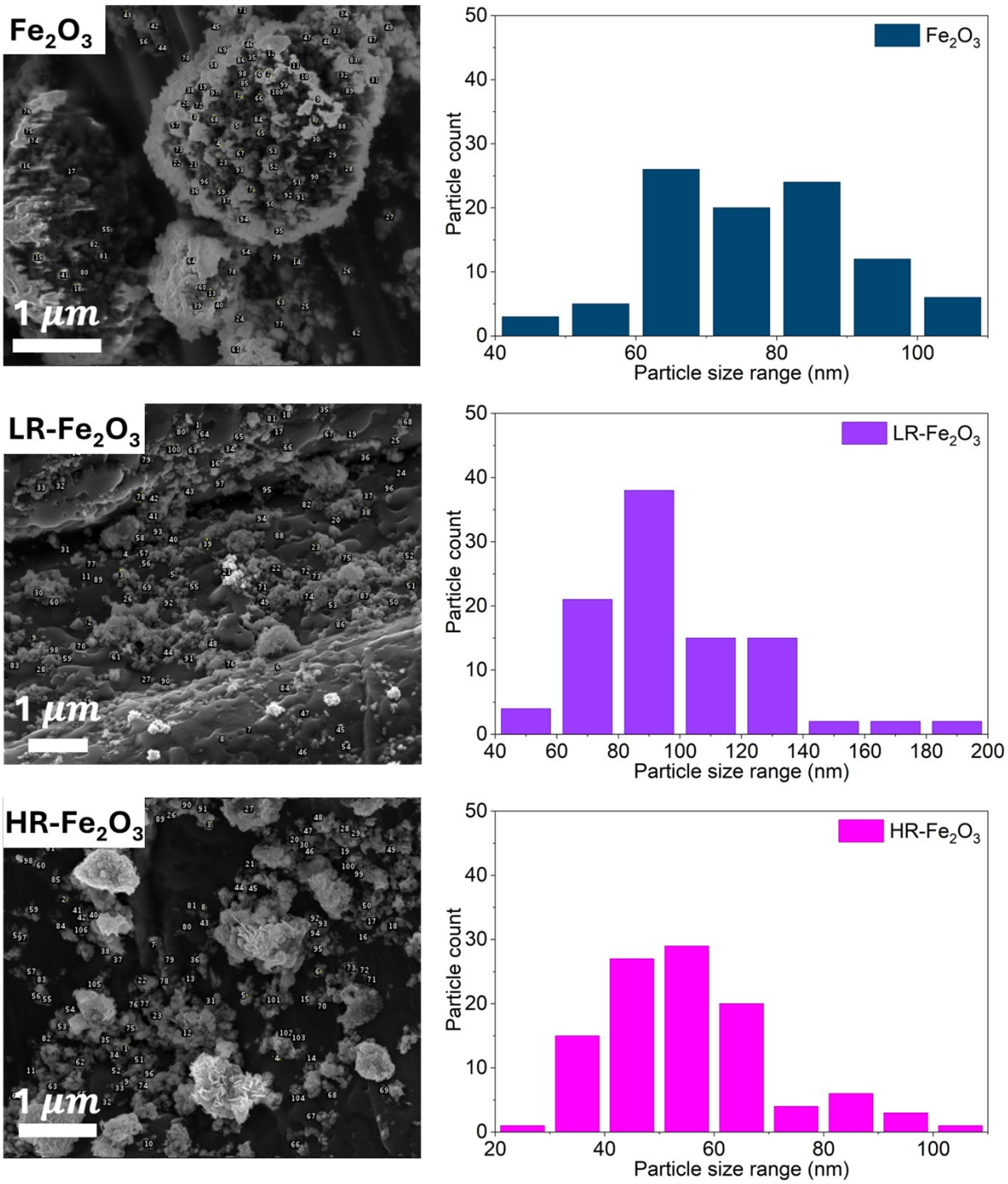

Figure S15. The SEM images of Fe_2O_3, LR-Fe_2O_3, and HR-Fe_2O_3 samples and particle size distributions of the randomly selected area within the SEM images. Fe_2O_3 primarily consists of nanoparticles with sizes in the range of 60 to 100 nm. LR-Fe_2O_3 exhibits similar nanoparticle sizes (60 to 100 nm), along with the presence of flake-like aggregates formed by particle assembly. HR-Fe_2O_3 displays relatively smaller nanoparticles (40 to 70 nm) and also shows more flake-like aggregation than LR-Fe_2O_3.

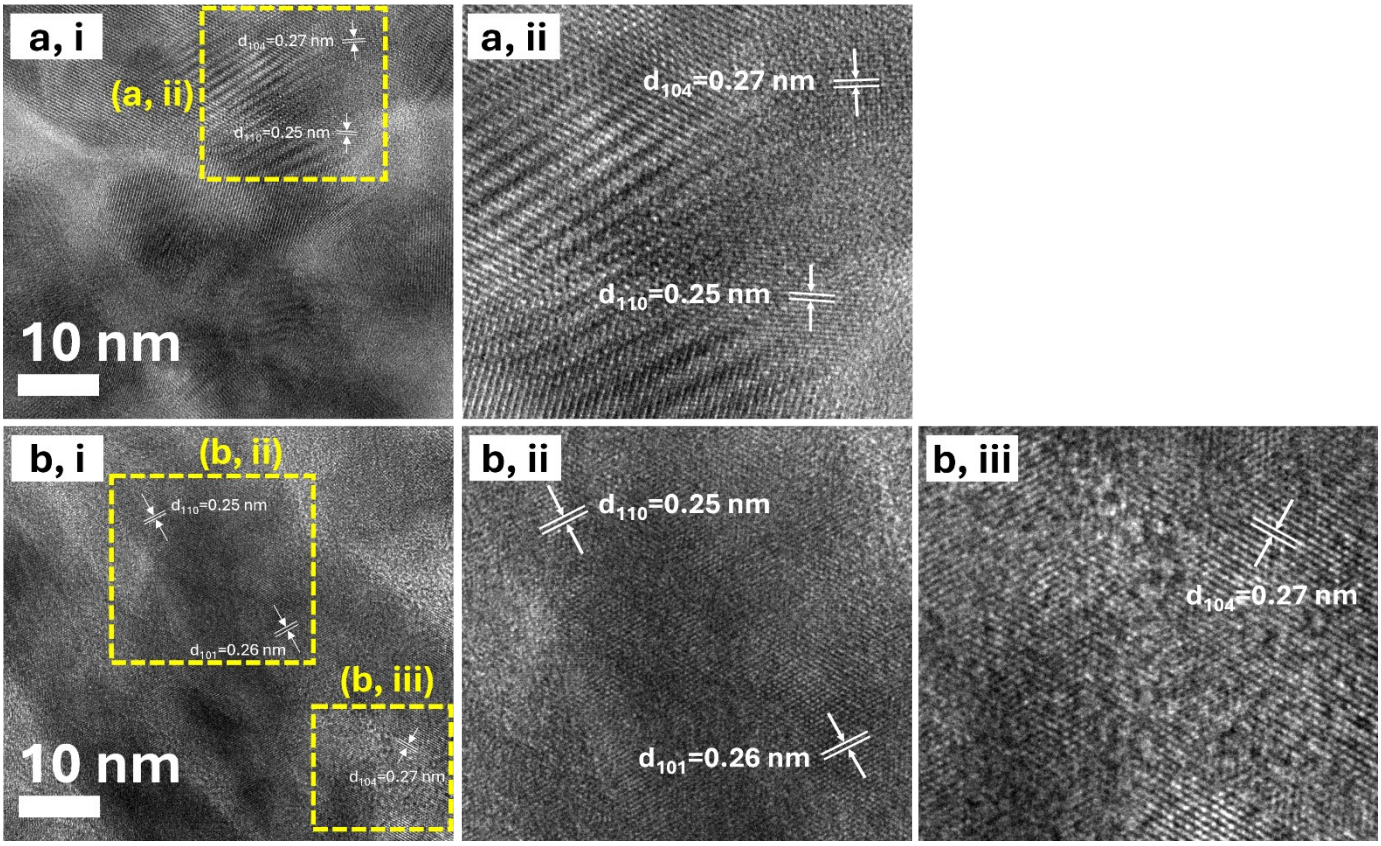

Figure S16. High-resolution TEM (HR-TEM) images of **(a)** pristine Fe_2O_3 and **(b)** LR- Fe_2O_3 at **(i)** a magnification of 10 nm, with **(ii)** and **(iii)** showing enlarged views of specific areas indicated in **(i)**. The results show all samples demonstrate lattice spacings of 0.27 and 0.25 nm corresponding to the (104) and (110) planes of α-Fe_2O_3, respectively.[1,4] Additionally, both LR-Fe_2O_3 display a lattice spacing of 0.26 nm, which corresponds to the (101) plane of α-Fe_2O_3.

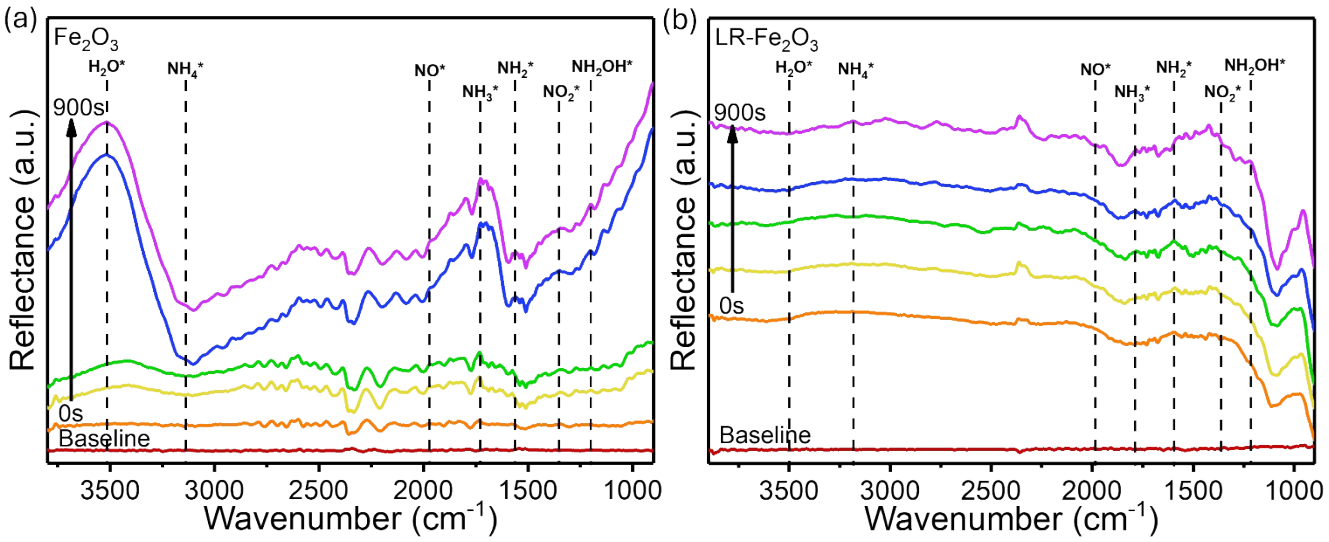

Figure S17. *In situ* FTIR spectra of **(a)** Fe_2O_3 and **(b)** LR-Fe_2O_3 at NO_2RR applied potential of -1.0 V vs RHE for 15 mins in electrolyte condition of 0.1 M KOH + 0.1 M KNO_2. The results reveal peaks corresponding to various intermediates: NH_2OH* (1215 cm^{-1}), NO_2* (1362 cm^{-1}), NH_2* (1563 cm^{-1}), NH_3* (1767 cm^{-1}), NO* (1971 cm^{-1}), NH_4* (3142 cm^{-1}), and H_2O* (3500 cm^{-1}).[5–14]

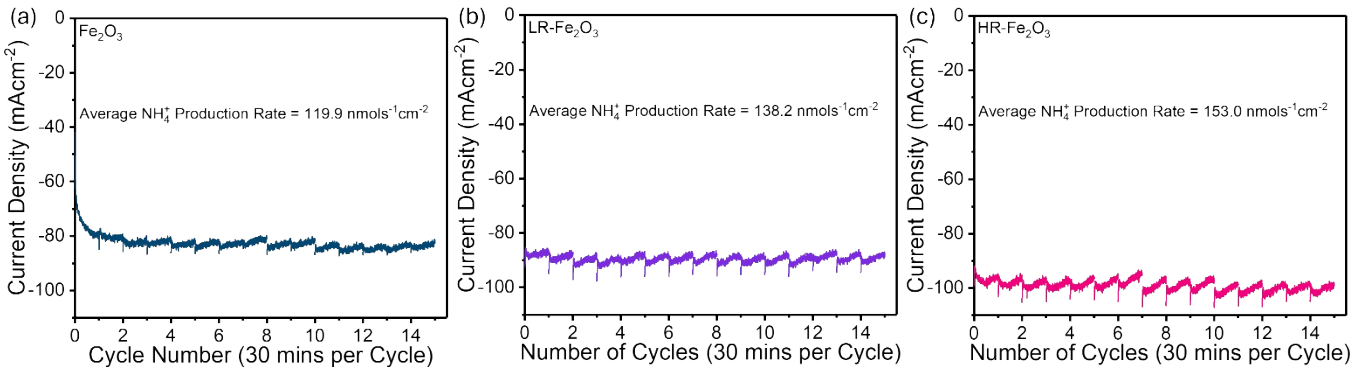

Figure S18. Chronoamperometric *i-t* curves of 15-cycle test (30 mins each cycle) of all electrodes at -1.0 V vs RHE: **(a)** Fe_2O_3, **(b)** LR-Fe_2O_3, and **(c)** HR-Fe_2O_3. All electrodes demonstrate high NO_2RR activity over prolonged periods, confirming their stability. Among them, HR-Fe_2O_3 catalyst exhibits the highest NO_2RR performance, achieving an average NH_4^+ production rate of 153.0 nmol s^{-1} cm^{-2} and FE_{NH4+} of 93%.

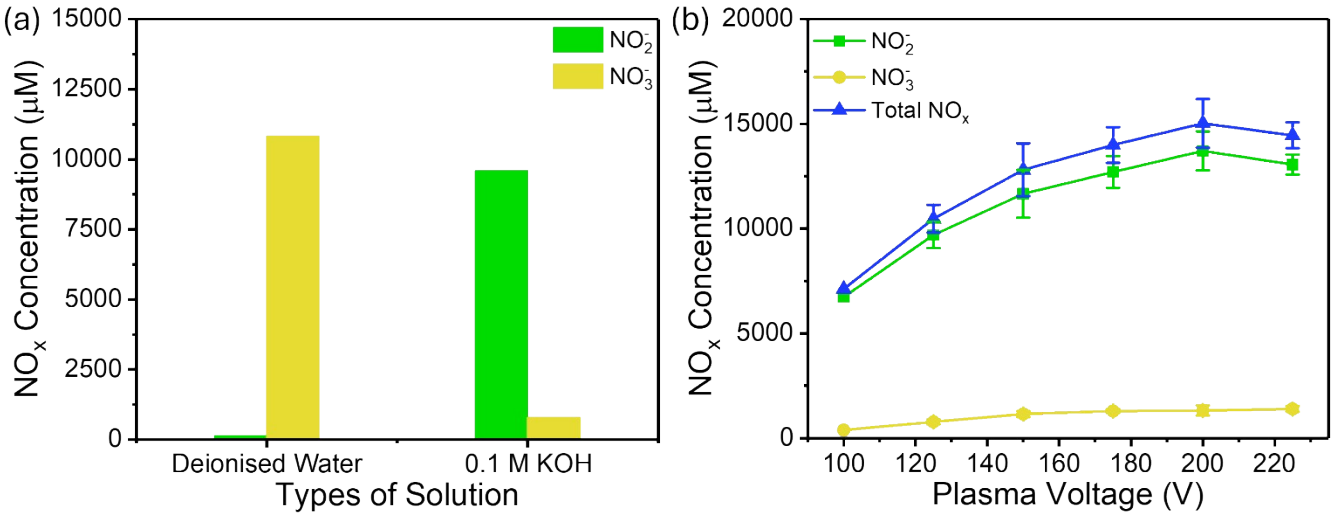

Figure S19. Production of NO_x via plasma system at varying **(a)** electrolyte pH conditions (neutral vs alkaline) and **(b)** plasma voltage under constant plasma operating conditions of 66 μS duty, 900 Hz discharge frequency, and 60 kHz resonance frequency. The results indicate that the alkaline condition (0.1 M KOH) significantly favors the production of NO_2^- (9.6 mM) over NO_3^- (0.8 mM), whereas in neutral environments, the production trends reverse, favoring NO_3^- over NO_2^-. In addition, the results indicate that the highest amounts of NO_2^- and total NO_x are produced at 200 V, with concentrations of 13.7 and 15.0 mM, respectively.

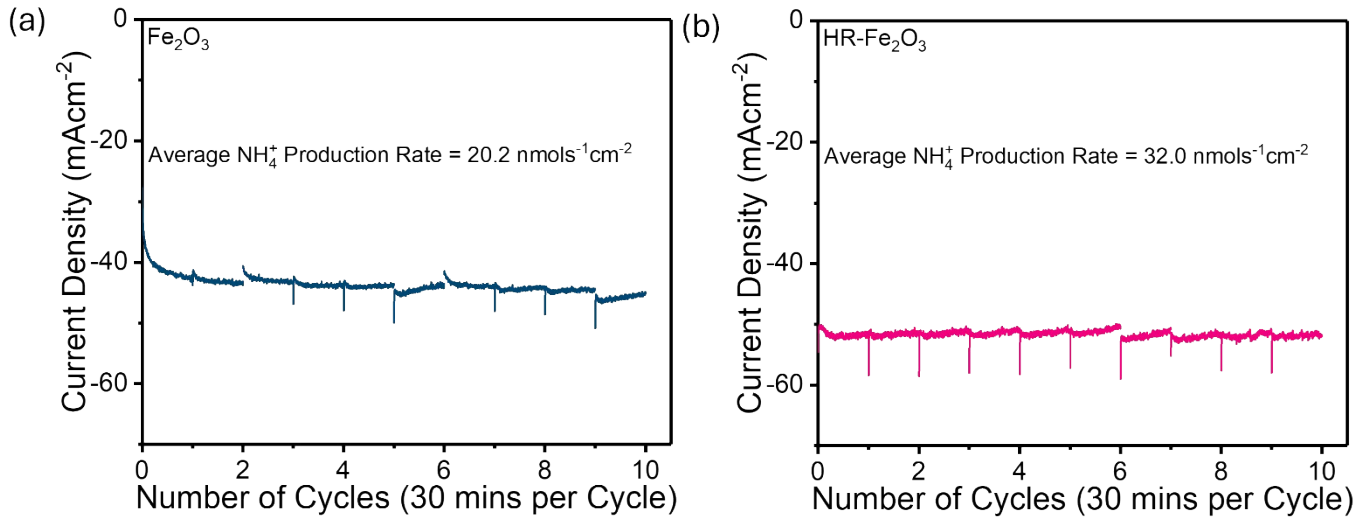

Figure S20. Chronoamperometric *i-t* curves of 10-cycle test (30 mins each cycle) of **(a)** Fe_2O_3 and **(b)** HR-Fe_2O_3 electrodes at -1.0 V vs RHE in PAAE electrolyte. The results demonstrate the high stability of both Fe_2O_3 and HR-Fe_2O_3 across the 10-cycle operation at -1.0 V vs RHE. The results also suggest that HR-Fe_2O_3 outperforms pristine Fe_2O_3 under low NO_x concentrations, achieving a stable NH_4^+ production rate of 32.0 nmol s^{-1} cm^{-2} and a steady current density of ~ 52 mA cm^{-2} across 10-cycle tests at -1.0 V vs RHE.

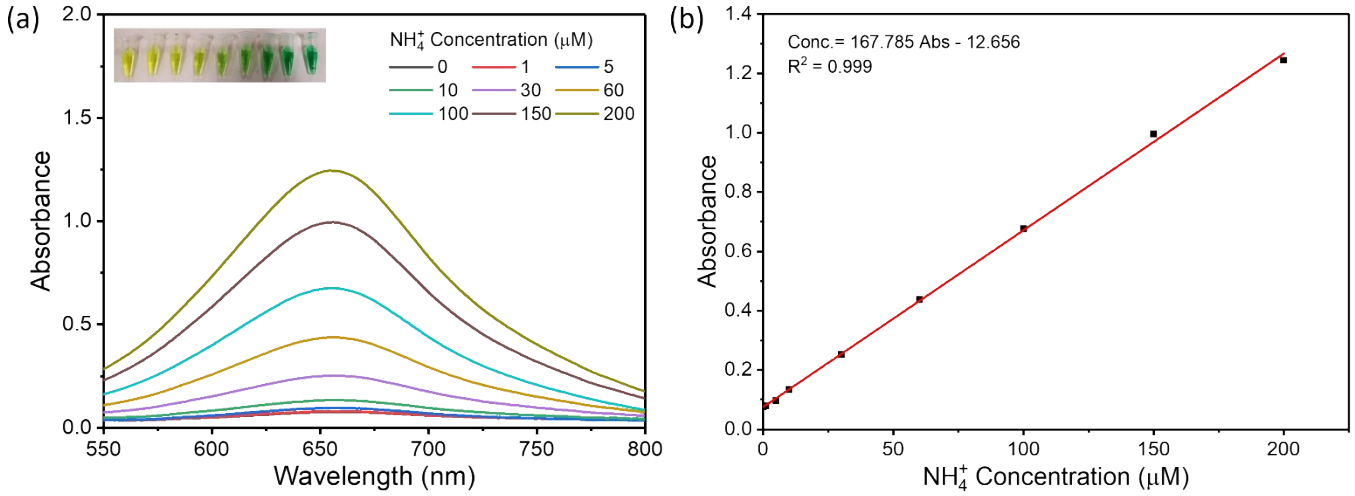

Figure S21. (a) UV-Vis absorption spectra with wavelengths ranging from 550 to 800 nm and its corresponding **(b)** NH_4^+ calibration curve of indophenol blue test using $(NH_4)_2SO_4$ standard solutions.

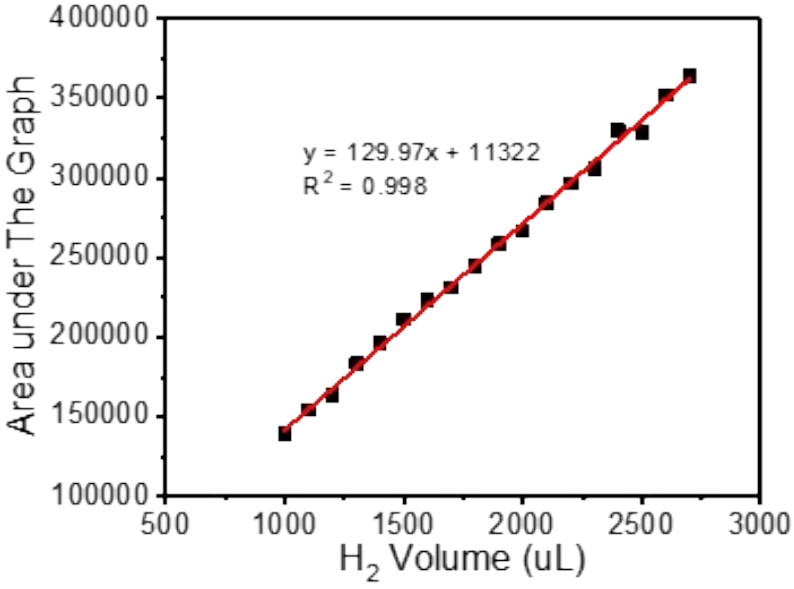

Figure S22. H_2 calibration curve produced with GC.

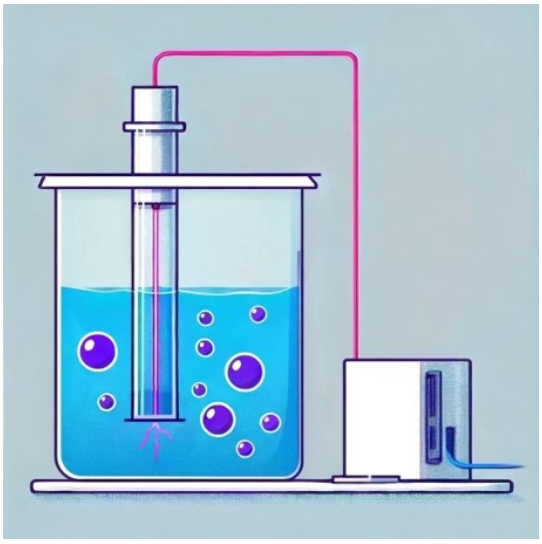

Figure S23. Illustration of the in-house, custom-built plasma system (as described in the work by Jing et al.[15]), comprising of a plasma generator ('Leap 100' from PlasmaLeap Technologies) and a plasma reactor.

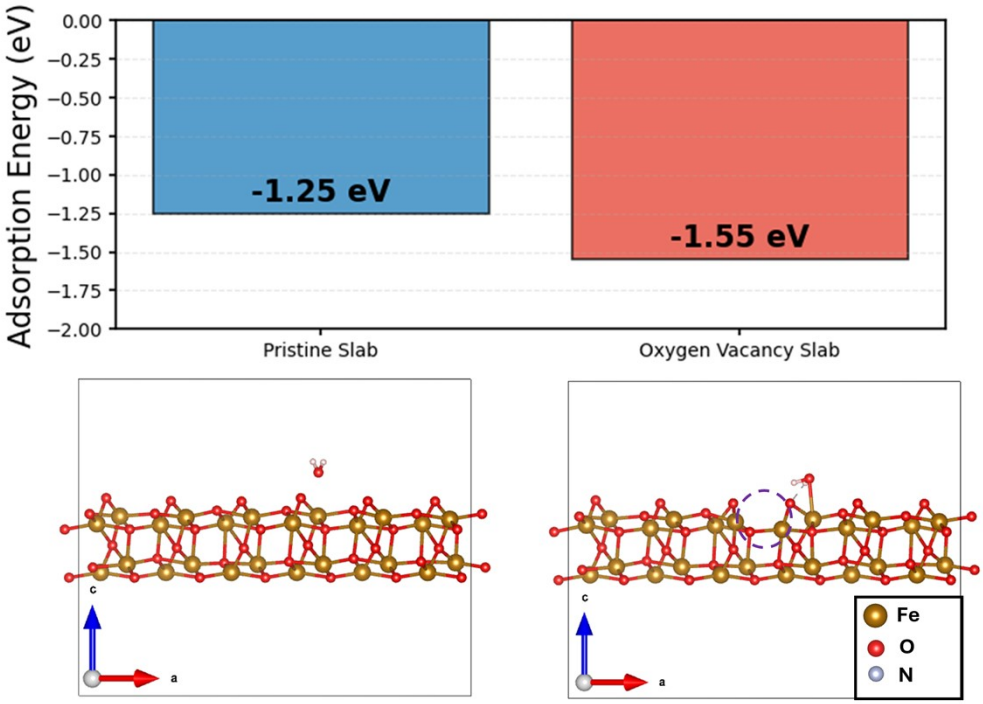

Figure S24. DFT calculated H_2O adsorption energies and optimized structural configurations on pristine and oxygen vacancy hematite (104) surfaces.

Supporting Tables

Table S1. Electrochemically active surface area (ECSAs) of Fe_2O_3, LR-Fe_2O_3, and HR-Fe_2O_3 electrodes. The final ECSAs were computed by having the specific capacitance in **Figure S6** divided by the reference blank glassy carbon (40 μFcm^{-2}), and then multiplied with geometric area.[16]

Electrode	ECSA (cm^2)
Fe_2O_3	6.1
LR-Fe_2O_3	5.1
HR-Fe_2O_3	6.7

Table S2. α-Fe_2O_3 crystallite (calculated via Scherrer equation) and lattice parameter (α-Fe_2O_3 d-spacing) of Fe_2O_3, LR-Fe_2O_3 and HR-Fe_2O_3. The results reveal no obvious trend or significant change in crystallite size and lattice spacing with different ERC potentials.

		Crystallite Size (nm)			d-spacing (Å)		
Sample	**Plane**	**(104)**	**(110)**	**(101)**	**(104)**	**(110)**	**(101)**
Fe_2O_3		18	22	-	2.710	2.526	-
LR-Fe_2O_3		18	26	19	2.710	2.526	2.559
HR-Fe_2O_3		20	23	26	2.710	2.527	2.560

Table S3. State-of-the-art NO_xRR-to-NH_3/NH_4^+ electrocatalysts.

Catalyst	Electrolyte	Potential (V_{RHE})	Current Density ($mA\ cm^{-2}$)	NH_3/NH_4^+ Yield ($nmol\ s^{-1}\ cm^{-2}$)	FE_{NH4+} (%)	Key Features	Ref.
HR-Fe_2O_3	0.1 M KOH + 0.1 M KNO_2	-1.0	~ 96.5 [(a)]	153	93	Disordered structure: $Fe^{3+}/Fe^{2+}/Fe$ interfaces and lattice strain	**This work**
a-RuO_2	0.5 M Na_2SO_4 + $NaNO_3$ (200 ppm NO_3^--N)	-0.35	NA	32.2	97.5	Disordered structure, oxygen vacancies	17
Ru-ST-12	1 M KOH + 1 M KNO_3	-0.20	~ 105 [(a)]	164	~ 100	Lattice strain	18
Pd (111)	0.1 M Na_2SO_4 + 0.1 M NO_3^-	-0.70	~ 130	152	79.9	Optimised NO_3^- adsorption energy	19
Cuboctahedron Pd/C	0.1 M NaOH + 20 mM $NaNO_3$	-0.20	4.25 [(b)]	7.51	35.1	Synergistic effects of Pd (111) and Pd (100)	20
Rh (110)	0.1 M KOH + 0.1 M KNO_3	0.10	NA	0.561	20.8	Rh (110) with optimised activation energy to convert N* to NH* RDS	21
SAC Rh_1	0.5 M Na_2SO_4 + 0.1 M $NaNO_2$	-0.70	~ 89.0	131	85.9	Enhanced activation and hydrogenation of NO_2RR	22
OD-Ag	0.1 M NO_3^- + 0.1 M KCl	-0.92	NA	NA	89.0	Enhanced ECSAs, Ag (211) with better NO_3* adsorption capabilities	23
Metastable phase Cu	1 M KOH + 0.05 M NO_3^-	-0.30	135 [(a)]	151	99.8	Shifted d-band centre closer to Fermi level	24
Cu-LC-10	0.5 M Na_2SO_4 + $NaNO_3$	-0.80	NA	173	94.7	Shifted d-band centre closer to Fermi level	25
u-Cu NWs	0.5 M Na_2SO_4 + 0.1 M $NaNO_2$	-0.70	~ 80.0	137	94.7	Shifted d-band centre closer to Fermi level	26
OD-Cu	0.1 M PBS + 0.1 M KNO_3	-0.90	NA	61.1	93.9	Cu^0 active sites	27
OD-Cu	1 M KOH + 100 mM NO_3^-	-0.15	NA	306	91.6	Cu^0 active sites	28
Cu nanodisks	0.1 M KOH + 10 mM KNO_3 And 0.1 M KOH + 10 mM KNO_2	-0.50 -0.50	NA	166 89.3	81.1 49.6	New, stable configuration of triatomic Cu clusters	29
e-Cu	1 M KOH + 50 mM KNO_3	-0.40	~ 33.5	~ 39.4	91.5	New, stable configuration of triatomic Cu clusters	30
OD-Cu: CuO- vs Cu_2O-derived Cu	0.5 M Na_2SO_4 + 100 mg/L NO_3^--N ($NaNO_3$)	-1.30	NA	86.1	80.0	*In situ* generated stacking faults, tensile strain	31
Cu_2O nanocubes	0.1 M Na_2SO_4 + 8 mM $NaNO_3$ And 0.1 M Na_2SO_4 + 8 mM $NaNO_2$	-0.30 -0.30	~ 16.0 NA	12.5 13.6	~ 88.0 91.5	Cu_2O/Cu interfaces	32
Cu/Cu_2O NWAs	0.5 M Na_2SO_4 + 200 ppm NO_3^--N ($NaNO_3$)	-0.85	100	68.0	95.8	Cu_2O/Cu interfaces, enhanced electron transfer	33

Table S3 (Continued). State-of-the-art NO_xRR-to-NH_3/NH_4^+ electrocatalysts.

Catalyst	Electrolyte	Potential (V_{RHE})	Current Density (mA cm^{-2})	NH_3/NH_4^+ Yield (nmol s^{-1} cm^{-2})	FE_{NH4+} (%)	Key Features	Ref.
Cu/Cu_2O/HTC-350	0.5 M Na_2SO_4 + 200 ppm NO_3^--N ($NaNO_3$)	-0.95	NA	3.92	89.5	Cu_2O/Cu interfaces, enhanced electron transfer	34
OVs-Cu/Cu_2O NRs	0.5 M Na_2SO_4 + 100 ppm NO_3^--N	-0.60	30.0	74.7	84.9	Oxygen vacancies, Cu_2O/Cu interfaces, synergistic effect of Cu and Cu_2O sites	35
R-Cu_2O/Cu/CF	1 M KOH + 250 mg/L NO_3^-	-0.25	14.0	35.4	84.4	Cu_2O/Cu interfaces, enhanced electron transfer	5
Cu NWAs	PAW + 0.01 M H_2SO_4 (PAW = 12 mM NO_3^-)	-0.60	NA	45.0	100	Synergistic effect of Cu^0/Cu^+ active sites, oxygen vacancies	15
$Cu_2O/Cu(OH)_2$	0.1 M KOH + 500 ppm NO_3^- (KNO_3)	-0.40	~ 9.00	153	77.0	Enhanced electron transfer, shifted d-band centre closer to Fermi level	36
FSP-CuO	0.05 M KNO_3 + 0.05 M H_2SO_4	-0.50	NA	~ 62.5	NA	Oxygen vacancies	37
CF@Cu_2O	0.1 M PBS + 0.1 M $NaNO_2$	-1.00	~ 40.0	122	94.2	Oxygen vacancies	38
dr-Cu NPs	0.5 M K_2SO_4 + 50 ppm KNO_3-N	-0.26	NA	12.6	85.5	Defect-rich	39
FOSP-Cu	0.1 M Na_2SO_4 + 0.1 M KNO_3	-0.27	NA	28.2	93.9	Open reaction environment, improved liquid-mass transfer	40
SAC Co_1/C_3N_4	0.5 M Na_2SO_4 + 0.1 M $NaNO_2$	-0.70	~ 65.0	112	95.7	Improved NO_2^- activation and optimised formation energy of NOH*	41
Different transition metal oxides: Co_3O_4 (highest)	1 M KOH + 0.3 M KNO_3	-0.25	NA	~ 278	85.2	Unique physiochemical properties, optimised electronic structure	42
OH-derived Co NAs	1 M KOH + 0.1 M NO_3^- (KNO_3)	-0.14	~ 900	1156	100	Improved conductivity, optimised adsorption energies	43
Co/CoO NSAs	0.1 M Na_2SO_4 + 200 ppm NO_3^--N ($NaNO_3$)	-0.26	NA	54.0	93.8	Co/CoO interfaces	44
OVs-Co_3O_4/Co-h	0.1 M Na_2SO_4 + 1 mg/mL NO_3^- (KNO_3)	-0.80	~ 60.0	72.2	88.7	Oxygen vacancies	45
OVs-Co_3O_{4-x}/Co	0.1 M PBS + 0.1 M KNO_2	-0.80	NA	136	97.0	Oxygen vacancies	46
V_{Co}-Co_3O_4/CC	0.1 M NaOH + 0.1 M $NaNO_3$	-0.40	40.0 [a]	108	97.2	Co vacancies	47
Fe SAC	0.1 M K_2SO_4 + 0.5 M KNO_3	-0.66	35.3 [a]	34.2	~ 75.0	Lacking neighbouring metal sites, suppressed N_2 formation	48
Fe_2O_3 NRs/CC	0.5 M Na_2SO_4 + 0.1 M $NaNO_3$	-0.90	~ 125	91.2	69.8	Improved ECSAs and electron transport	49
450°C-Fe_2O_3/CC	0.5 M Na_2SO_4 + 0.1 M $NaNO_3$	-0.96	~ 97.0	91.2	84.9	Greatest amounts of low valence Fe, enhanced electron transfer to activate NO_3^-	50

Table S3 (Continued). State-of-the-art NO_xRR-to-NH_3/NH_4^+ electrocatalysts.

Catalyst	Electrolyte	Potential (V_{RHE})	Current Density (mA cm^{-2})	NH_3/NH_4^+ Yield (nmol s^{-1} cm^{-2})	FE_{NH4+} (%)	Key Features	Ref.
NA-FeOOH/SS	0.1 M PBS + 0.5 M Na_2SO_4 + 0.2 M $NaNO_3$	-0.69	~ 87.0	11.9	99.6	Fe^{2+} active sites	51
OVs-FeOOH/CP	0.1 M PBS + 0.1 M $NaNO_3$	-0.50	~ 12.0	14.7	92.0	Oxygen vacancies	52
δ-FeOOH	0.25 M PBS + 500 ppm NO_3^--N	-1.00	~ 56.0 (a)	70.1	90.2	Enhanced hydrogenation ability with NO_x* intermediates	53
3D FeOOH NTA/CC	0.1 M PBS + 0.1 M $NaNO_2$	-1.00	~ 95.0	163	94.7	3D self-standing nanotube array structure, enhanced ECSAs and electron transport	54
Zero-valent Fe (ZVI)	NaOH + 200 mg NO_3^--N/L	NA	NA	NA	NA	Fe/Fe^{2+} system	55
Ti foil	0.1 M HNO_3 + 0.3 M KNO_3	-1.00	22.0 (a)	NA	82.0	High corrosion resistance	56
OVs-TiO_{2-x} nanotubes	0.5 M Na_2SO_4 + 50 ppm NO_3^--N ($NaNO_3$)	-0.56	NA	25.0	85.0	Oxygen vacancies	57
OVs-TiO_{2-x} NBA/Ti plate	0.1 M NaOH + 0.1 M NO_2^- And 0.1 M K_2SO_4 + 0.1 M NO_2^-	-0.70 -0.50	~ 85.0 ~ 12.0	129 24.5	92.7 92.5	Oxygen vacancies	58
$Ni(OH)_2$@Ni	0.1 M Na_2SO_4 + 70 mg/L NO_3^--N	NA	25.0	NA	90.4	$Ni(OH)_2$ nanoparticles	59
V_{Ni}-Ni-NSA	0.2 M Na_2SO_4 + 200 ppm NO_2^--N (200 mg/L $NaNO_2$)	-0.16	NA	68.4	88.9	Ni vacancies	60
MoO_2/Mo plate	0.5 M Na_2SO_4 + 0.1 M $NaNO_2$	-0.80	~ 100	142	94.5	MoO_2 (111)	61
Cu-Pt-180s	12.5 mM Na_2SO_4 + 30 mg NO_3^--N/L	NA	40	NA	~ 22.0	Cu/Pt interfaces synergistic effects	62
SAC Rh@Cu-0.6% NWs	0.1 M Na_2SO_4 + 0.1 M KNO_3	-0.20	162 (a)	353	93.0	Synergistic interactions between Rh and Cu sites	63
Ru-Cu NW (d)	1 M KOH + 2000 ppm NO_3^-	-0.017	~ 590 (a)	~ 750	96.0	Synergistic interactions between Ru and Cu sites	64
V_{Cu}-Au_1Cu SAAs	0.1 M KOH + 7.14 mM NO_3^- (KNO_3)	-0.20	~ 3.00	9.05	98.7	Electron-deficient Cu surface, Cu vacancies	65
Strain-defect AuCu@Ag NWs	0.1 M KOH + 50 mg/L NO_3^--N	-0.20	NA	15.9	96.9	Strain	66
PdCu/Cu_2O	0.5 M Na_2SO_4 + 100 ppm NO_3^--N ($NaNO_3$)	-0.80	NA	52.8	94.3	Synergistic interactions between electron-deficient Pd and Cu sites	67

Table S3 (Continued). State-of-the-art NO_xRR-to-NH_3/NH_4^+ electrocatalysts.

Catalyst	Electrolyte	Potential (V_{RHE})	Current Density (mA cm^{-2})	NH_3/NH_4^+ Yield (nmol s^{-1} cm^{-2})	FE_{NH4+} (%)	Key Features	Ref.
Pd-Cu_2O CEO	0.5 M K_2SO_4 + 50 ppm KNO_3	-1.70	NA	15.1	96.6	Corner-etched cavity structure, oxygen vacancies, synergistic interaction between Pd and Cu_2O active sites	68
1D PdCuAg MTs	0.1 M KOH + 10 mM KNO_3	-0.45	~ 25.0	43.3	95.2	Ample ECSAs, electron-rich surface, nanoconfinement microenvironment	69
Cu_2Pd/CBC	Plasma treated 0.5 M KOH	-0.10	~ 12.0	~ 17.1	93.8	Improved adsorption energies	70
Pd/CuO NOs	0.1 M K_2SO_4 + 0.01 M KNO_2	-0.46	~ 18.0	14.8	91.8	Pd/CuO interfaces, built-in electric field, porous structure	71
SAC $CuRh_1$	0.5 M Na_2SO_4 + 0.1 M $NaNO_2$	-0.60	~ 80.0	125	94.1	Synergistic interaction between Rh_1 and Cu sites	72
$CuCo_2O_4$/CFs	1 M KOH + 0.1 M KNO_3	-0.30	~ 40.0	43.8	81.9	$CuCo_2O_4$ nanoparticles active sites, porous carbon nanofibers substrate	73
OVs-$CuCo_2O_4$/CuO	0.1 M PBS + 0.1 M KNO_3	-0.90	~ 120	153	95.1	Oxygen vacancies	74
Cu_1Co_5	1 M KOH + 1 M KNO_3	0.075	453 [a]	NA	96.2	Synergistic interaction between Co and Cu sites	75
Co_3O_4@CuO	0.1 M KOH + 0.1 M KNO_2	-0.31	~ 49.0	75.2	92.4	Synergistic interaction between Co_3O_4 and CuO sites	76
$Cu_{50}Co_{50}$/Ni foam [d]	1 M KOH + 100 mM KNO_3	-0.20	1035	1333	100	Synergistic interaction between Co and Cu sites	6
NiCo LDH/Cu NW	1 M KOH + 2000 ppm NO_3^-	-0.21	570 [a]	~ 653	94.3	Synergistic interaction between Cu and NiCo layered double hydroxide sites	77
$Cu_{50}Ni_{50}$/Cu foam	1 M KOH + 0.1 M KNO_3	-0.10	-90.0	NA	> 95.0	Enhanced NO_3^- adsorption, shifted d-band centre closer to Fermi level	78
Island-like Cu/Ni foam	0.5 M Na_2SO_4 + 50 mM KNO_3	-0.80	NA	~ 97.2	98.3	Cu_2O active sites, island-like morphology with faults and defects	79
Janus Cu@Ni	1 M KOH + 100 mM KNO_3	-0.20	~ 31.5	62.6	92.5	Synergistic interaction between Ni and Cu sites	80
OVs-Cu-Fe_2O_3-60/Cu foam	0.5 M Na_2SO_4 + 50 ppm NO_3^--N ($NaNO_3$)	-0.60	NA	30.0	80.1	Cu/Fe_2O_3 interfaces, oxygen vacancies	81
Cu-doped Fe_3O_4 flakes	0.1 M KOH + 0.1 M KNO_3	-0.60	~ 92.0	225	~ 100	Altered electronic structure, improved adsorption energies	82
Cu@TiO_2/Ti plate	0.1 M Na_2SO_4 + 0.1 M $NaNO_2$	-0.60	~ 85.0	141	95.3	Cu/TiO_2 interfaces, enhanced charge transfer	83
Cu_1/MnO_2	0.5 M Na_2SO_4 + 0.1 M $NaNO_2$	-0.70	~ 80.0	122	93.3	Cu single-atom active sites	84

Table S3 (Continued). State-of-the-art NO_xRR-to-NH_3/NH_4^+ electrocatalysts.

Catalyst	Electrolyte	Potential (V_{RHE})	Current Density ($mA\ cm^{-2}$)	NH_3/NH_4^+ Yield ($nmol\ s^{-1}\ cm^{-2}$)	FE_{NH4+} (%)	Key Features	Ref.
$Ru_{15}Co_{85}$ HNDs	0.1 M KNO_3 + 0.1 M KOH	+0.40	NA	535	97.0	Altered electronic properties, improved NO_3^- activation and adsorption	10
RuO_x-Co_3O_4	0.1 M Na_2SO_4 + 0.5 M KNO_3	-0.60	65.8 [(a)]	58.5	89.7	Synergistic interaction between Co and Ru sites	85
SAC Co_1Ru	0.5 M Na_2SO_4 + 0.1 M $NaNO_2$	-0.70	~ 82.0	132	94.2	Co_1-Ru heteronuclear active sites	86
Co_3O_4/Ni foam	1.0 M NaOH + 0.1 M $NaNO_3$	-0.60	~ 920 [(a)]	~ 1207	99.3	Improved ECSAs and electron transfer channels, electron-deficient Co_3O_4 active sites	87
$(Co_{0.83}Ni_{0.16})_2Fe$ LDOs	1 M KOH + 0.1 M KNO_3	-0.42	590 [(a)]	822	97.8	Synergistic interaction between Co and Ni sites	88
Co_3O_4/NiO CF	0.5 M Na_2SO_4 + 100 ppm $NaNO_2$	-0.59	NA	5.28	99.4	Co_3O_4/NiO interfaces	89
Fe-doped Co_3O_4 NA/TM	0.1 M PBS + 50 mM NO_3^-	-0.70	~10.0	10.6	95.5	Altered coordination environment, improved conductivity and NO_3^- adsorption	90
3D flower-like $ZnCo_2O_4$	0.1 M KOH + 0.1 M KNO_3	-0.40	~ 7.00	8.97	95.4	Improved ECSAs, charge transfer	91
Co@TiO_2/TP	0.1 M PBS + 0.1 M NO_3^-	-0.70	~ 75.0	103	96.7	Improved ECSAs, Co/TiO_2 interfaces, built-in electric field	92
2000 ppm Ru-Fe_2O_3	0.5 M Na_2SO_4 + 0.1 M $NaNO_3$	-0.90	~ 100	91.4	72.8	Improved hydrogenation	93
OVs-0.01Ru-$NiMoO_4$/Ni foam	0.5 M Na_2SO_4 + 0.1 M $NaNO_2$	-0.60	~ 180	280	95.6	Oxygen vacancies	94
SAC Ni_1Ru	0.5 M Na_2SO_4 + 0.1 M $NaNO_2$	-0.60	~ 85.0	135	95.9	Optimised electronic structure	95
Ru-TiO_2/Ti plate	0.1 M NaOH + 0.1 M $NaNO_2$	-0.50	~ 180	~ 283	98.9	Improved electron conductivity and charge transfer	96
Ni@TiO_2/Ti plate	0.1 M NaOH + 0.1 M $NaNO_2$	-0.50	~ 90.0	158	98.5	Schottky junction, Ni/TiO2 interfaces	97
Ni-TiO_2/Ti plate	0.1 M NaOH + 0.1 M $NaNO_2$	-0.50	~ 65.0	107	94.9	Improved electrical conductivity and adsorption energies	98
Ni foam/Ti plate	0.1 M PBS + 0.1 M $NaNO_2$	-0.80	~ 132	206	95.9	3D porous structure with cauliflower-like morphology, improved ECSAs and electrical conductivity	99
OVs-Zr-TiON	0.5 M Na_2SO_4 + 0.05 M KNO_3	NA	60.0	73.7	94.8	Unsaturated Zr sites, oxygen vacancies	100
OVs-Fe_2TiO_5	PBS + 0.1 M $NaNO_3$ And PBS + 0.1 M $NaNO_2$	-1.0 -0.90	~ 26.0 ~ 25.0	20.3 37.8	87.6 96.1	Oxygen vacancies	101
Ag@TiO_2/Ti plate	0.1 M NaOH + 0.1 M NO_2^-	-0.50	~ 85.0	143	96.4	Improved ECSAs	102

Table S3 (Continued). State-of-the-art NO_xRR-to-NH_3/NH_4^+ electrocatalysts.

Catalyst	Electrolyte	Potential (V_{RHE})	Current Density ($mA\ cm^{-2}$)	NH_3/NH_4^+ Yield ($nmol\ s^{-1}\ cm^{-2}$)	FE_{NH4+} (%)	Key Features	Ref.
V-TiO_2/Ti plate	0.1 M NaOH + 0.1 M NO_2^-	-0.60	~ 72.0	116	93.2	Improved electrical conductivity, optimised electronic properties	[103]
Pd-TiO_2/CC	1 M LiCl + 0.25 M $LiNO_3^-$	-0.70	20.0	17.1	92.1	Altered electronic structure, optimised adsorption energies	[104]
SAC Nb_1-ZrO_2	0.5 M Na_2SO_4 + 0.1 M $NaNO_2$	-0.60	~ 87.5	124	95.1	Synergistic interaction between $Nb1_1$ and ZrO_2 sites	[105]
SAC Mo_1-ZrO_2	0.5 M Na_2SO_4 + 0.1 M $NaNO_2$	-0.70	~ 60.0	96.4	94.8	Single atom Mo active sites	[106]
Nb-NiO	0.5 M Na_2SO_4 + 0.1 M $NaNO_2$	-0.60	~ 28.0	55.7	92.4	Nb Lewis acid active sites	[107]
Ag@NiO/CC	0.1 M NaOH + 0.1 M $NaNO_2$	-0.40	~ 38.5	65.2	97.7	Ag (100) active sites	[108]

a- The reported current density reported is partial current density for NH_3/NH_4^+ production.

b- The reported current density (or partial) was normalised to ECSAs.

c- Computational study only.

d- The NH_3/NH_4^+ production performance was conducted in a flow cell instead of H-cell.

e- Abbreviations: (1) FE_{NH4+} is Faradaic efficiency for NH_3/NH_4^+ production.
(2) Ref. is reference.
(3) PBS is phosphate buffered saline.

References

(1) Li, P. X.; Qu, L.-M.; Zhang, C.-H.; Ren, X.-B.; Wang, H.-X.; Zhang, J.-L.; Mu, Y.-W.; Lü, B.-L. Probing into the Crystal Plane Effect on the Reduction of α-Fe2O3 in CO by Operando Raman Spectroscopy. *J. Fuel Chem. Technol.* **2021**, *49* (10), 1558–1566. https://doi.org/10.1016/S1872-5813(21)60154-8.

(2) Frankcombe, T. J.; Liu, Y. Interpretation of Oxygen 1s X-Ray Photoelectron Spectroscopy of ZnO. *Chem. Mater.* **2023**, *35* (14), 5468–5474. https://doi.org/10.1021/acs.chemmater.3c00801.

(3) Biesinger, M. C.; Payne, B. P.; Grosvenor, A. P.; Lau, L. W. M.; Gerson, A. R.; Smart, R. S. C. Resolving Surface Chemical States in XPS Analysis of First Row Transition Metals, Oxides and Hydroxides: Cr, Mn, Fe, Co and Ni. *Appl. Surf. Sci.* **2011**, *257* (7), 2717–2730. https://doi.org/10.1016/j.apsusc.2010.10.051.

(4) Fu, Y. Y.; Wang, R. M.; Xu, J.; Chen, J.; Yan, Y.; Narlikar, A. V.; Zhang, H. Synthesis of Large Arrays of Aligned α-Fe2O3 Nanowires. *Chem. Phys. Lett.* **2003**, *379* (3–4), 373–379. https://doi.org/10.1016/j.cplett.2003.08.061.

(5) Fu, W.; Hu, Z.; Zheng, Y.; Su, P.; Zhang, Q.; Jiao, Y.; Zhou, M. Tuning Mobility of Intermediate and Electron Transfer to Enhance Electrochemical Reduction of Nitrate to Ammonia on Cu2O/Cu Interface. *Chem. Eng. J.* **2022**, *433*, 133680. https://doi.org/10.1016/j.cej.2021.133680.

(6) Fang, J.-Y.; Zheng, Q.-Z.; Lou, Y.-Y.; Zhao, K.-M.; Hu, S.-N.; Li, G.; Akdim, O.; Huang, X.-Y.; Sun, S.-G. Ampere-Level Current Density Ammonia Electrochemical Synthesis Using CuCo Nanosheets Simulating Nitrite Reductase Bifunctional Nature. *Nat. Commun.* **2022**, *13* (1), 7899. https://doi.org/10.1038/s41467-022-35533-6.

(7) Chu, K.; Luo, Y.; Shen, P.; Li, X.; Li, Q.; Guo, Y. Unveiling the Synergy of O-Vacancy and Heterostructure over MoO3-x/MXene for N2 Electroreduction to NH3. *Adv. Energy Mater.* **2022**, *12* (3), 2103022. https://doi.org/10.1002/aenm.202103022.

(8) Barbosa, A. I.; Costa Lima, S. A.; Reis, S. Application of PH-Responsive Fucoidan/Chitosan Nanoparticles to Improve Oral Quercetin Delivery. *Molecules* **2019**, *24* (2), 346. https://doi.org/10.3390/molecules24020346.

(9) Al-Abduly, A.; Christensen, P. An in Situ and Downstream Study of Non-Thermal Plasma Chemistry in an Air Fed Dielectric Barrier Discharge (DBD). *Plasma Sources Sci. Technol.* **2015**, *24* (6), 065006. https://doi.org/10.1088/0963-0252/24/6/065006.

(10) Han, S.; Li, H.; Li, T.; Chen, F.; Yang, R.; Yu, Y.; Zhang, B. Ultralow Overpotential Nitrate Reduction to Ammonia via a Three-Step Relay Mechanism. *Nat. Catal.* **2023**, *6* (5), 402–414. https://doi.org/10.1038/s41929-023-00951-2.

(11) Alenazi, N.; Hussein, M.; Alamry, K.; Asiri, A. Nanocomposite-Based Aminated Polyethersulfone and Carboxylate Activated Carbon for Environmental Application. A Real Sample Analysis. *J. Carbon Res.* **2018**, *4* (2), 30. https://doi.org/10.3390/c4020030.

(12) Karelin, A. I.; Kayumov, R. R.; Dobrovolsky, Y. A. FTIR Spectroscopic Study of the Interaction between NH4+ and DMSO in Nafion. *Spectrochim. Acta Part A Mol. Biomol. Spectrosc.* **2019**, *215*, 381–388. https://doi.org/10.1016/j.saa.2019.03.007.

(13) Verma, S. K.; Deb, M. K. Nondestructive and Rapid Determination of Nitrate in Soil, Dry Deposits and Aerosol Samples Using KBr-Matrix with Diffuse Reflectance Fourier Transform Infrared Spectroscopy (DRIFTS). *Anal. Chim. Acta* **2007**, *582* (2), 382–389. https://doi.org/10.1016/j.aca.2006.09.020.

(14) Lim, M.; Ma, Z.; O'Connell, G.; Yuwono, J. A.; Kumar, P.; Jalili, R.; Amal, R.; Daiyan, R.; Lovell, E. C. Ru-Induced Defect Engineering in Co3O4 Lattice for High Performance Electrochemical Reduction of Nitrate to Ammonium. *Small* **2024**, *20* (33), 2401333. https://doi.org/10.1002/smll.202401333.

(15) Sun, J.; Alam, D.; Daiyan, R.; Masood, H.; Zhang, T.; Zhou, R.; Cullen, P. J.; Lovell, E. C.; Jalili, A.; Amal, R. A Hybrid Plasma Electrocatalytic Process for Sustainable Ammonia Production. *Energy Environ. Sci.* **2021**, *14* (2), 865–872. https://doi.org/10.1039/d0ee03769a.

(16) Ma, Z.; Tsounis, C.; Toe, C. Y.; Kumar, P. V.; Subhash, B.; Xi, S.; Yang, H. Y.; Zhou, S.; Lin, Z.; Wu, K. H.; Wong, R. J.; Thomsen, L.; Bedford, N. M.; Lu, X.; Ng, Y. H.; Han, Z.; Amal, R. Reconstructing Cu Nanoparticle Supported on Vertical Graphene Surfaces via Electrochemical Treatment to Tune the Selectivity of CO2 Reduction toward Valuable Products. *ACS Catal.* **2022**, *12* (9), 4792–4805. https://doi.org/10.1021/acscatal.1c05431.

(17) Wang, Y.; Li, H.; Zhou, W.; Zhang, X.; Zhang, B.; Yu, Y. Structurally Disordered RuO2 Nanosheets with Rich Oxygen Vacancies for Enhanced Nitrate Electroreduction to Ammonia. *Angew. Chemie* **2022**, *134* (19), e20220204. https://doi.org/10.1002/anie.202202604.

(18) Li, J.; Zhan, G.; Yang, J.; Quan, F.; Mao, C.; Liu, Y.; Wang, B.; Lei, F.; Li, L.; Chan, A. W. M.; Xu, L.; Shi, Y.; Du, Y.; Hao, W.; Wong, P. K.; Wang, J.; Dou, S.-X.; Zhang, L.; Yu, J. C. Efficient Ammonia Electrosynthesis from Nitrate on Strained Ruthenium Nanoclusters. *J. Am. Chem. Soc.* **2020**, *142* (15), 7036–7046. https://doi.org/10.1021/jacs.0c00418.

(19) Han, Y.; Zhang, X.; Cai, W.; Zhao, H.; Zhang, Y.; Sun, Y.; Hu, Z.; Li, S.; Lai, J.; Wang, L. Facet-Controlled Palladium Nanocrystalline for Enhanced Nitrate Reduction towards Ammonia. *J. Colloid Interface Sci.* **2021**, *600*, 620–628. https://doi.org/10.1016/j.jcis.2021.05.061.

(20) Lim, J.; Liu, C.-Y.; Park, J.; Liu, Y.-H.; Senftle, T. P.; Lee, S. W.; Hatzell, M. C. Structure Sensitivity of Pd Facets for Enhanced Electrochemical Nitrate Reduction to Ammonia. *ACS Catal.* **2021**, *11* (12), 7568–7577. https://doi.org/10.1021/acscatal.1c01413.

(21) Guo, Y.; Cai, X.; Shen, S.; Wang, G.; Zhang, J. Computational Prediction and Experimental Evaluation of Nitrate Reduction to Ammonia on Rhodium. *J. Catal.* **2021**, *402*, 1–9. https://doi.org/10.1016/j.jcat.2021.08.016.

(22) Xiang, J.; Zhao, H.; Chen, K.; Yang, X.; Chu, K. Electrocatalytic Nitrite Reduction to Ammonia on an Rh Single-Atom Catalyst. *J. Colloid Interface Sci.* **2024**, *659* (December 2023), 432–438. https://doi.org/10.1016/j.jcis.2024.01.013.

(23) Liu, H.; Park, J.; Chen, Y.; Qiu, Y.; Cheng, Y.; Srivastava, K.; Gu, S.; Shanks, B. H.; Roling, L. T.; Li, W. Electrocatalytic Nitrate Reduction on Oxide-Derived Silver with Tunable Selectivity to Nitrite and Ammonia. *ACS Catal.* **2021**, *11* (3), 8431–8442. https://doi.org/10.1021/acscatal.1c01525.

(24) Wen, W.; Yan, P.; Sun, W.; Zhou, Y.; Yu, X.-Y. Metastable Phase Cu with Optimized Local Electronic State for Efficient Electrocatalytic Production of Ammonia from Nitrate. *Adv. Funct. Mater.* **2023**, *33* (6), 2212236. https://doi.org/10.1002/adfm.202212236.

(25) Huang, K.; Tang, K.; Wang, M.; Wang, Y.; Jiang, T.; Wu, M. Boosting Nitrate to Ammonia via the Optimization of Key Intermediate Processes by Low-Coordinated Cu–Cu Sites. *Adv. Funct. Mater.* **2024**, *34* (24), 2315324. https://doi.org/10.1002/adfm.202315324.

(26) Zhang, R.; Shang, S.; Wang, F.; Chu, K. Electrocatalytic Reduction of Nitrite to Ammonia on Undercoordinated Cu. *Dalt. Trans.* **2024**, *53* (8), 3470–3475. https://doi.org/10.1039/d4dt00043a.

(27) Zhou, N.; Wang, Z.; Zhang, N.; Bao, D.; Zhong, H.; Zhang, X. Potential-Induced Synthesis and Structural Identification of Oxide-Derived Cu Electrocatalysts for Selective Nitrate Reduction to Ammonia. *ACS Catal.* **2023**, *13* (11), 7529–7537. https://doi.org/10.1021/acscatal.3c01315.

(28) Yuan, J.; Xing, Z.; Tang, Y.; Liu, C. Tuning the Oxidation State of Cu Electrodes for Selective Electrosynthesis of Ammonia from Nitrate. *ACS Appl. Mater. Interfaces* **2021**, *13* (44), 52469–52478. https://doi.org/10.1021/acsami.1c10946.

(29) Wu, K.; Sun, C.; Wang, Z.; Song, Q.; Bai, X.; Yu, X.; Li, Q.; Wang, Z.; Zhang, H.; Zhang, J.; Tong, X.; Liang, Y.; Khosla, A.; Zhao, Z. Surface Reconstruction on Uniform Cu Nanodisks Boosted Electrochemical Nitrate Reduction to Ammonia. *ACS Mater. Lett.* **2022**, *4* (4), 650–656.

https://doi.org/10.1021/acsmaterialslett.2c00149.

(30) Kim, Y.; Ko, J.; Shim, M.; Park, J.; Shin, H.-H.; Kim, Z. H.; Jung, Y.; Byon, H. R. Identifying the Active Sites and Intermediates on Copper Surfaces for Electrochemical Nitrate Reduction to Ammonia. *Chem. Sci.* **2024**, *15* (7), 2578–2585. https://doi.org/10.1039/d3sc05793c.

(31) Fang, L.; Wang, S.; Song, C.; Lu, S.; Yang, X.; Qi, X.; Liu, H. Boosting Nitrate Electroreduction to Ammonia via in Situ Generated Stacking Faults in Oxide-Derived Copper. *Chem. Eng. J.* **2022**, *446*, 137341. https://doi.org/10.1016/j.cej.2022.137341.

(32) Bai, L.; Franco, F.; Timoshenko, J.; Rettenmaier, C.; Scholten, F.; Jeon, H. S.; Yoon, A.; Rüscher, M.; Herzog, A.; Haase, F. T.; Kühl, S.; Chee, S. W.; Bergmann, A.; Beatriz, R. C. Electrocatalytic Nitrate and Nitrite Reduction toward Ammonia Using Cu2O Nanocubes: Active Species and Reaction Mechanisms. *J. Am. Chem. Soc.* **2024**, *146* (14), 9665–9678. https://doi.org/10.1021/jacs.3c13288.

(33) Wang, Y.; Zhou, W.; Jia, R.; Yu, Y.; Zhang, B. Unveiling the Activity Origin of a Copper-Based Electrocatalyst for Selective Nitrate Reduction to Ammonia. *Angew. Chemie Int. Ed.* **2020**, *59* (13), 5350–5354. https://doi.org/10.1002/anie.201915992.

(34) Ma, A.; Wu, X.; Li, X.; Dewi Susanti, Y.; Liu, D.; Li, H.; Kuvarega, A. T.; Mamba, B. B.; Gui, J. Electrocatalytic Nitrate Reduction to Ammonia over Cu/Cu2O Catalysts with Controllable Ratios. *Appl. Surf. Sci.* **2024**, *653*, 159397. https://doi.org/10.1016/j.apsusc.2024.159397.

(35) Shi, Y.; Li, Y.; Li, R.; Zhao, X.; Yu, Y.; Yang, M. In-Situ Reconstructed Cu/Cu2O Heterogeneous Nanorods with Oxygen Vacancies for Enhanced Electrocatalytic Nitrate Reduction to Ammonia. *Chem. Eng. J.* **2024**, *479*, 147574. https://doi.org/10.1016/j.cej.2023.147574.

(36) Geng, J.; Ji, S. Boosting Electrocatalytic Nitrate Reduction to Ammonia via Cu2O/Cu(OH)2 Heterostructures Promoting Electron Transfer. *Nano Res.* **2024**, *17* (6), 4898–4907. https://doi.org/10.1007/s12274-024-6480-1.

(37) Daiyan, R.; Tran-Phu, T.; Kumar, P.; Iputera, K.; Tong, Z.; Leverett, J.; Khan, M. H. A.; Asghar Esmailpour, A.; Jalili, A.; Lim, M.; Tricoli, A.; Liu, R.-S.; Lu, X.; Lovell, E.; Amal, R. Nitrate Reduction to Ammonium: From CuO Defect Engineering to Waste NOx-to-NH3 Economic Feasibility. *Energy Environ. Sci.* **2021**, *14* (6), 3588–3598. https://doi.org/10.1039/d1ee00594d.

(38) Chen, Q.; An, X.; Liu, Q.; Wu, X.; Xie, L.; Zhang, J.; Yao, W.; Hamdy, M. S.; Kong, Q.; Sun, X. Boosting Electrochemical Nitrite-Ammonia Conversion Properties by a Cu Foam@Cu2O Catalyst. *Chem. Commun.* **2022**, *58* (4), 517–520. https://doi.org/10.1039/d1cc06215h.

(39) Xu, Y.; Wang, M.; Ren, K.; Ren, T.; Liu, M.; Wang, Z.; Li, X.; Wang, L.; Wang, H. Atomic Defects in Pothole-Rich Two-Dimensional Copper Nanoplates Triggering Enhanced Electrocatalytic Selective Nitrate-to-Ammonia Transformation. *J. Mater. Chem. A* **2021**, *9* (30), 16411–16417. https://doi.org/10.1039/d1ta04743d.

(40) Zhao, Y.; Liu, Y.; Zhang, Z.; Mo, Z.; Wang, C.; Gao, S. Flower-like Open-Structured Polycrystalline Copper with Synergistic Multi-Crystal Plane for Efficient Electrocatalytic Reduction of Nitrate to Ammonia. *Nano Energy* **2022**, *97*, 107124. https://doi.org/10.1016/j.nanoen.2022.107124.

(41) Zhao, H.; Xiang, J.; Sun, Z.; Shang, S.; Chu, K. Electroreduction of Nitrite to Ammonia over a Cobalt Single-Atom Catalyst. *ACS Sustain. Chem. Eng.* **2024**, *12* (7), 2783–2789. https://doi.org/10.1021/acssuschemeng.3c07388.

(42) Wu, Q.; Zhu, W.; Ma, D.; Liang, C.; Wang, Z.; Liang, H. Screening of Transition Metal Oxides for Electrocatalytic Nitrate Reduction to Ammonia at Large Currents. *Nano Res.* **2024**, *17* (5), 3902–3910.

(43) Deng, X.; Yang, Y.; Wang, L.; Fu, X.-Z.; Luo, J.-L. Metallic Co Nanoarray Catalyzes Selective NH3 Production from Electrochemical Nitrate Reduction at Current Densities Exceeding 2 A Cm-2. *Adv. Sci.* **2021**, *8* (7), 2004523. https://doi.org/10.1002/advs.202004523.

(44) Yu, Y.; Wang, C.; Yu, Y.; Wang, Y.; Zhang, B. Promoting Selective Electroreduction of Nitrates to

Ammonia over Electron-Deficient Co Modulated by Rectifying Schottky Contacts. *Sci. China Chem.* **2020**, *63* (10), 1469–1476. https://doi.org/10.1007/s11426-020-9795-x.

(45) Zhao, F.; Hai, G.; Li, X.; Jiang, Z.; Wang, H. Enhanced Electrocatalytic Nitrate Reduction to Ammonia on Cobalt Oxide Nanosheets via Multiscale Defect Modulation. *Chem. Eng. J.* **2023**, *461*, 141960. https://doi.org/10.1016/j.cej.2023.141960.

(46) Shi, S.-S.; Yuan, Z.-X.; Zhang, F.; Chen, P. A Co3O4-x/Co Nanocomposite with Synergistically Enhanced Electrochemical Activity for Reduction of Nitrite to Ammonia. *Electrochim. Acta* **2024**, *473*, 143455. https://doi.org/10.1016/j.electacta.2023.143455.

(47) Deng, Z.; Ma, C.; Li, Z.; Luo, Y.; Zhang, L.; Sun, S.; Liu, Q.; Du, J.; Lu, Q.; Zheng, B.; Sun, X. High-Efficiency Electrochemical Nitrate Reduction to Ammonia on a Co3O4 Nanoarray Catalyst with Cobalt Vacancies. *ACS Appl. Mater. Interfaces* **2022**, *14* (41), 46595–46602. https://doi.org/10.1021/acsami.2c12772.

(48) Wu, Z.-Y.; Karamad, M.; Yong, X.; Huang, Q.; Cullen, D. A.; Zhu, P.; Xia, C.; Xiao, Q.; Shakouri, M.; Chen, F.-Y.; Kim, J. Y. (Timothy); Xia, Y.; Heck, K.; Hu, Y.; Wong, M. S.; Li, Q.; Gates, I.; Siahrostami, S.; Wang, H. Electrochemical Ammonia Synthesis via Nitrate Reduction on Fe Single Atom Catalyst. *Nat. Commun.* **2021**, *12* (1), 2870. https://doi.org/10.1038/s41467-021-23115-x.

(49) Li, T.; Tang, C.; Guo, H.; Wu, H.; Duan, C.; Wang, H.; Zhang, F.; Cao, Y.; Yang, G.; Zhou, Y. In Situ Growth of Fe2O3 Nanorod Arrays on Carbon Cloth with Rapid Charge Transfer for Efficient Nitrate Electroreduction to Ammonia. *ACS Appl. Mater. Interfaces* **2022**, *14* (44), 49765–49773. https://doi.org/10.1021/acsami.2c14215.

(50) Li, T.; Tang, C.; Guo, H.; Yang, J.; Zhang, F.; Yang, G.; Zhou, Y. Understanding First Electron Transfer Kinetic Process of Electrochemical Nitrate Reduction to Ammonia on Fe2O3 Nanorods Array. *Chem. Eng. J.* **2024**, *485*, 149560. https://doi.org/10.1016/j.cej.2024.149560.

(51) Liu, C.; Zhang, G.; Zhang, W.; Gu, Z.; Zhu, G. Specifically Adsorbed Ferrous Ions Modulate Interfacial Affinity for High-Rate Ammonia Electrosynthesis from Nitrate in Neutral Media. *Proc. Natl. Acad. Sci.* **2023**, *120* (3), e2209979120. https://doi.org/10.1073/pnas.

(52) Liu, Q.; Liu, Q.; Xie, L.; Ji, Y.; Li, T.; Zhang, B.; Li, N.; Tang, B.; Liu, Y.; Gao, S.; Luo, Y.; Yu, L.; Kong, Q.; Sun, X. High-Performance Electrochemical Nitrate Reduction to Ammonia under Ambient Conditions Using a FeOOH Nanorod Catalyst. *ACS Appl. Mater. Interfaces* **2022**, *14* (15), 17312–17318. https://doi.org/10.1021/acsami.2c00436.

(53) Qu, K.; Zhu, X.; Zhang, Y.; Song, L.; Wang, J.; Gong, Y.; Liu, X.; Wang, A.-L. Enhancing Nitrate Reduction to Ammonia Through Crystal Phase Engineering: Unveiling the Hydrogen Bonding Effect in δ-FeOOH Electrocatalysis. *Small* **2024**, *20* (31), 2401327. https://doi.org/10.1002/smll.202401327.

(54) Liu, Q.; Liu, Q.; Xie, L.; Yue, L.; Li, T.; Luo, Y.; Li, N.; Tang, B.; Yu, L.; Sun, X. A 3D FeOOH Nanotube Array: An Efficient Catalyst for Ammonia Electrosynthesis by Nitrite Reduction. *Chem. Commun.* **2022**, *58* (33), 5160–5163. https://doi.org/10.1039/d2cc00611a.

(55) Xiang, H.; Liu, W.; Su, L.; Chen, S.; Han, Y.; Zhu, C.; Wang, S.; Tan, C.; Zhang, L. Nitrate Reduction to Ammonia in Fe/Fe2+ System: A Case Study on the Mechanism of Green Rust Generation. *Sep. Purif. Technol.* **2024**, *330*, 125357. https://doi.org/10.1016/j.seppur.2023.125357.

(56) McEnaney, J. M.; Blair, S. J.; Nielander, A. C.; Schwalbe, J. A.; Koshy, D. M.; Cargnello, M.; Jaramillo, T. F. Electrolyte Engineering for Efficient Electrochemical Nitrate Reduction to Ammonia on a Titanium Electrode. *ACS Sustain. Chem. Eng.* **2020**, *8* (7), 2672–2681. https://doi.org/10.1021/acssuschemeng.9b05983.

(57) Jia, R.; Wang, Y.; Wang, C.; Ling, Y.; Yu, Y.; Zhang, B. Boosting Selective Nitrate Electroreduction to Ammonium by Constructing Oxygen Vacancies in TiO2. *ACS Catal.* **2020**, *10* (6), 3533–3540. https://doi.org/10.1021/acscatal.9b05260.

(58) Zhao, D.; Liang, J.; Li, J.; Zhang, L.; Dong, K.; Yue, L.; Luo, Y.; Ren, Y.; Liu, Q.; Hamdy, M. S.; Li,

Q.; Kong, Q.; Sun, X. A TiO2-x Nanobelt Array with Oxygen Vacancies: An Efficient Electrocatalyst toward Nitrite Conversion to Ammonia. *Chem. Commun.* **2022**, *58* (22), 3669–3672. https://doi.org/10.1039/d2cc00856d.

(59) Zheng, W.; Zhu, L.; Yan, Z.; Lin, Z.; Lei, Z.; Zhang, Y.; Xu, H.; Dang, Z.; Wei, C.; Feng, C. Self-Activated Ni Cathode for Electrocatalytic Nitrate Reduction to Ammonia: From Fundamentals to Scale-Up for Treatment of Industrial Wastewater. *Environ. Sci. Technol.* **2021**, *55* (19), 13231–13243. https://doi.org/10.1021/acs.est.1c02278.

(60) Wang, C.; Zhou, W.; Sun, Z.; Wang, Y.; Zhang, B.; Yu, Y. Integrated Selective Nitrite Reduction to Ammonia with Tetrahydroisoquinoline Semi-Dehydrogenation over a Vacancy-Rich Ni Bifunctional Electrode. *J. Mater. Chem. A* **2021**, *9* (1), 239–243. https://doi.org/10.1039/d0ta09590g.

(61) Wang, G.; Chen, Q.; An, X.; Liu, Q.; Xie, L.; Zhang, J.; Yao, W.; Liu, X.; Sun, S.; Sun, X.; Kong, Q. Ambient Ammonia Production via Electrocatalytic Nitrite Reduction over MoO2 Nanoparticles Self-Supported on Molybdenum Plate. *Colloids Surfaces A Physicochem. Eng. Asp.* **2023**, *657*, 130549. https://doi.org/10.1016/j.colsurfa.2022.130549.

(62) Cerrón-Calle, G. A.; Fajardo, A. S.; Sánchez-Sánchez, C. M.; Garcia-Segura, S. Highly Reactive Cu-Pt Bimetallic 3D-Electrocatalyst for Selective Nitrate Reduction to Ammonia. *Appl. Catal. B Environ.* **2022**, *302*, 120844. https://doi.org/10.1016/j.apcatb.2021.120844.

(63) Liu, H.; Lang, X.; Zhu, C.; Timoshenko, J.; Ruscher, M.; Bai, L.; Guijarro, N.; Yin, H.; Peng, Y.; Li, J.; Liu, Z.; Wang, W.; Cuenya, B. R.; Luo, J. Efficient Electrochemical Nitrate Reduction to Ammonia with Copper-Supported Rhodium Cluster and Single-Atom Catalysts. *Angew. Chemie Int. Ed.* **2022**, *61* (23), e202202556.

(64) Chen, F.-Y.; Wu, Z.-Y.; Gupta, S.; Rivera, D. J.; Lambeets, S. V.; Pecaut, S.; Kim, J. Y. T.; Zhu, P.; Finfrock, Y. Z.; Meira, D. M.; King, G.; Gao, G.; Xu, W.; Cullen, D. A.; Zhou, H.; Han, Y.; Perea, D. E.; Muhich, C. L.; Wang, H. Efficient Conversion of Low-Concentration Nitrate Sources into Ammonia on a Ru-Dispersed Cu Nanowire Electrocatalyst. *Nat. Nanotechnol.* **2022**, *17* (7), 759–767. https://doi.org/10.1038/s41565-022-01121-4.

(65) Zhang, Y.; Chen, X.; Wang, W.; Yin, L.; Crittenden, J. C. Electrocatalytic Nitrate Reduction to Ammonia on Defective Au1Cu (111) Single-Atom Alloys. *Appl. Catal. B Environ.* **2022**, *310*, 121346. https://doi.org/10.1016/j.apcatb.2022.121346.

(66) Liu, S.; Miao, W.; Ma, K.; Teng, H.; Zhang, X.; Li, J.; Li, W.; Cui, X.; Jiang, L. Defect-Rich AuCu@Ag Nanowires with Exclusive Strain Effect Accelerate Nitrate Reduction to Ammonia. *Appl. Catal. B Environ. Energy* **2024**, *350*, 123919. https://doi.org/10.1016/j.apcatb.2024.123919.

(67) Yin, H.; Chen, Z.; Xiong, S.; Chen, J.; Wang, C.; Wang, R.; Kuwahara, Y.; Luo, J.; Yamashita, H.; Peng, Y.; Li, J. Alloying Effect-Induced Electron Polarization Drives Nitrate Electroreduction to Ammonia. *Chem Catal.* **2021**, *1* (5), 1088–1103. https://doi.org/10.1016/j.checat.2021.08.014.

(68) Xu, Y.; Ren, K.; Ren, T.; Wang, M.; Wang, Z.; Li, X.; Wang, L.; Wang, H. Ultralow-Content Pd in-Situ Incorporation Mediated Hierarchical Defects in Corner-Etched Cu2O Octahedra for Enhanced Electrocatalytic Nitrate Reduction to Ammonia. *Appl. Catal. B Environ.* **2022**, *306*, 121094. https://doi.org/10.1016/j.apcatb.2022.121094.

(69) Sun, L.; Yao, H.; Wang, Y.; Zheng, C.; Liu, B. Mesostructures Engineering to Promote Selective Nitrate-to-Ammonia Electroreduction. *Adv. Energy Mater.* **2023**, *13* (44), 2303054. https://doi.org/10.1002/aenm.202303054.

(70) Li, W.; Zhang, S.; Ding, J.; Liu, J.; Wang, Z.; Zhang, H.; Ding, J.; Chen, L.; Liang, C. Sustainable Nitrogen Fixation to Produce Ammonia by Electroreduction of Plasma-Generated Nitrite. *ACS Sustain. Chem. Eng.* **2023**, *11* (3), 1168–1177. https://doi.org/10.1021/acssuschemeng.2c06525.

(71) Liu, S.; Cui, L.; Yin, S.; Ren, H.; Wang, Z.; Xu, Y.; Li, X.; Wang, L.; Wang, H. Heterointerface-Triggered Electronic Structure Reformation: Pd/CuO Nano-Olives Motivate Nitrite Electroreduction to Ammonia. *Appl. Catal. B Environ.* **2022**, *319*, 121876.

https://doi.org/10.1016/j.apcatb.2022.121876.

(72) Xiang, J.; Qiang, C.; Shang, S.; Chen, K.; Kang, C.; Chu, K. Tandem Electrocatalytic Reduction of Nitrite to Ammonia on Rhodium–Copper Single Atom Alloys. *Adv. Funct. Mater.* **2024**, *34* (36), 2401941. https://doi.org/10.1002/adfm.202401941.

(73) Niu, Z.; Fan, S.; Li, X.; Wang, P.; Liu, Z.; Wang, J.; Bai, C.; Zhang, D. Bifunctional Copper-Cobalt Spinel Electrocatalysts for Efficient Tandem-like Nitrate Reduction to Ammonia. *Chem. Eng. J.* **2022**, *450*, 138343. https://doi.org/10.1016/j.cej.2022.138343.

(74) Liu, X.; Cheng, X.; Zhao, H.; Liu, P.; Wang, Y.-Q. CuCo2O4/CuO Heterostructure with Oxygen Vacancies Induced by Plasma for Electrocatalytic Nitrate Reduction to Ammonia. *Inorg. Chem.* **2024**, *63* (30), 14093–14102. https://doi.org/10.1021/acs.inorgchem.4c01924.

(75) Zhou, Y.; Duan, R.; Li, H.; Zhao, M.; Ding, C.; Li, C. Boosting Electrocatalytic Nitrate Reduction to Ammonia via Promoting Water Dissociation. *ACS Catal.* **2023**, *13* (16), 10846–10854. https://doi.org/10.1021/acscatal.3c02951.

(76) Zhou, Y.; Meng, Y.; Wang, X.; Luo, J.; Xia, H.; Li, W.; Zhang, J. Enhancing Electro-Reduction of Nitrite to Ammonia by Loading Co3O4 on CuO to Construct Elecrocatalytic Dual-Sites. *Dalt. Trans.* **2023**, *52* (11), 3260–3264. https://doi.org/10.1039/d2dt03720c.

(77) Zhang, X.; Liu, X.; Huang, Z.-F.; Guo, L.; Gan, L.; Zhang, S.; Ajmal, M.; Pan, L.; Shi, C.; Zhang, X.; Yang, G.; Zou, J.-J. Tandem Nitrate Electroreduction to Ammonia with Industrial-Level Current Density on Hierarchical Cu Nanowires Shelled with NiCo-Layered Double Hydroxide. *ACS Catal.* **2023**, *13* (22), 14670–14679. https://doi.org/10.1021/acscatal.3c04541.

(78) Wang, Y.; Xu, A.; Wang, Z.; Huang, L.; Li, J.; Li, F.; Wicks, J.; Luo, M.; Nam, D.-H.; Tan, C.-S.; Ding, Y.; Wu, J.; Lum, Y.; Dinh, C.-T.; Sinton, D.; Zheng, G.; Sargent, E. H. Enhanced Nitrate-to-Ammonia Activity on Copper-Nickel Alloys via Tuning of Intermediate Adsorption. *J. Am. Chem. Soc.* **2020**, *142* (12), 5702–5708. https://doi.org/10.1021/jacs.9b13347.

(79) Wang, C.; Ye, F.; Shen, J.; Xue, K.-H.; Zhu, Y.; Li, C. In Situ Loading of Cu2O Active Sites on Island-like Copper for Efficient Electrochemical Reduction of Nitrate to Ammonia. *ACS Appl. Mater. Interfaces* **2022**, *14* (5), 6680–6688. https://doi.org/10.1021/acsami.1c21691.

(80) Lou, Y.-Y.; Zheng, Q.-Z.; Zhou, S.-Y.; Fang, J.-Y.; Akdim, O.; Ding, X.-Y.; Oh, R.; Park, G.-S.; Huang, X.; Sun, S.-G. Phase-Dependent Electrocatalytic Nitrate Reduction to Ammonia on Janus Cu@Ni Tandem Catalyst. *ACS Catal.* **2024**, *14* (7), 5098–5108. https://doi.org/10.1021/acscatal.4c00479.

(81) Gao, Y.; Huang, K.; Yan, C.; Li, S.; Zhang, H.; Cheng, L.; Huang, F. Interfacial Engineering of Cu-Fe2O3 Nanotube Arrays with Built-in Electric Field and Oxygen Vacancies for Boosting the Electrocatalytic Reduction of Nitrates. *Mater. Adv.* **2022**, *3* (18), 7107–7115. https://doi.org/10.1039/d2ma00685e.

(82) Wang, J.; Wang, Y.; Cai, C.; Liu, Y.; Wu, D.; Wang, M.; Li, M.; Wei, X.; Shao, M.; Gu, M. Cu-Doped Iron Oxide for the Efficient Electrocatalytic Nitrate Reduction Reaction. *Nano Lett.* **2023**, *23* (5), 1897–1903. https://doi.org/10.1021/acs.nanolett.2c04949.

(83) Ouyang, L.; Fan, X.; Li, Z.; He, X.; Sun, S.; Cai, Z.; Luo, Y.; Zheng, D.; Ying, B.; Zhang, J.; Alshehri, A. A.; Wang, Y.; Ma, K.; Sun, X. High-Efficiency Electroreduction of Nitrite to Ammonia on a Cu@TiO2 Nanobelt Array. *Chem. Commun.* **2023**, *59* (12), 1625–1628. https://doi.org/10.1039/d2cc06261e.

(84) Wan, Y.; Du, W.; Chen, K.; Zhang, N.; Chu, K. Electrocatalytic Nitrite-to-Ammonia Reduction on Isolated Cu Sites. *J. Colloid Interface Sci.* **2023**, *652*, 2180–2185. https://doi.org/10.1016/j.jcis.2023.09.071.

(85) Liu, Y.; Jiang, X.; Zhang, Y.; Li, H.; Huang, W.; Yang, Y.; Ye, M.; Liu, Y. The Interface-Mediated Electron Structure Tuning of RuOx-Co3O4 Nano-Particles for Efficient Electrocatalytic Nitrate

Reduction. *Dalt. Trans.* **2024**, *53* (1), 162–170. https://doi.org/10.1039/d3dt03318j.

(86) Wang, F.; Xiang, J.; Zhang, G.; Chen, K.; Chu, K. Single-Atom Co Alloyed Ru for Electrocatalytic Nitrite Reduction to Ammonia. *Nano Res.* **2024**, *17* (5), 3660–3666. https://doi.org/10.1007/s12274-023-6261-2.

(87) Zhao, D.; Yao, J.; Ma, C.; Wang, A.; Xie, H.; Zhao, J.; Yan, J.; Zhu, K.; Zhu, Y.; Cao, D.; Wang, G. 3D Integrated Non-Noble Metal Oxides Nano Arrays for Enhanced Nitrate Electroreduction to Ammonia. *J. Power Sources* **2024**, *592*, 233945. https://doi.org/10.1016/j.jpowsour.2023.233945.

(88) Yang, Q.; Bu, Y.; Pu, S.; Chu, L.; Huang, W.; Zhu, X.; Liu, C.; Fang, G.; Cui, P.; Zhou, D.; Wang, Y. Matched Kinetics Process Over Fe2O3-Co/NiO Heterostructure Enables Highly Efficient Nitrate Electroreduction to Ammonia. *Angew. Chemie Int. Ed.* **2024**, *63* (15), e202400428. https://doi.org/10.1002/anie.202400428.

(89) Begildayeva, T.; Theerthagiri, J.; Min, A.; Moon, C. J.; Choi, M. Y. Electrocatalytic Ammonia Production from Nitrite via Dual-Site Co3O4/NiO Catalysts Derived from Laser-Induced Cyanonickelate Frameworks. *Chem. Eng. J.* **2024**, *485*, 150041. https://doi.org/10.1016/j.cej.2024.150041.

(90) Wei, P.; Liang, J.; Liu, Q.; Xie, L.; Tong, X.; Ren, Y.; Li, T.; Luo, Y.; Li, N.; Tang, B.; Asiri, A. M.; Hamdy, M. S.; Kong, Q.; Wang, Z.; Sun, X. Iron-Doped Cobalt Oxide Nanoarray for Efficient Electrocatalytic Nitrate-to-Ammonia Conversion. *J. Colloid Interface Sci.* **2022**, *615*, 636–642. https://doi.org/10.1016/j.jcis.2022.01.186.

(91) Huang, P.; Fan, T.; Ma, X.; Zhang, J.; Zhang, Y.; Chen, Z.; Yi, X. 3D Flower-Like Zinc Cobaltite for Electrocatalytic Reduction of Nitrate to Ammonia under Ambient Conditions. *ChemSusChem* **2022**, *15* (4), e202102049. https://doi.org/10.1002/cssc.202102049.

(92) Fan, X.; Zhao, D.; Deng, Z.; Zhang, L.; Li, J.; Li, Z.; Sun, S.; Luo, Y.; Zheng, D.; Wang, Y.; Ying, B.; Zhang, J.; Alshehri, A. A.; Lin, Y.; Tang, C.; Sun, X.; Zheng, Y. Constructing Co@TiO2 Nanoarray Heterostructure with Schottky Contact for Selective Electrocatalytic Nitrate Reduction to Ammonia. *Small* **2023**, *19* (17), 2208036. https://doi.org/10.1002/smll.202208036.

(93) Luo, S.; Guo, H.; Li, T.; Wu, H.; Zhang, F.; Tang, C.; Chen, G.; Yang, G.; Zhou, Y. Ruthenium-Induced Hydrolysis Effect on Fe2O3 Nanoarrays for High-Performance Electrochemical Nitrate Reduction to Ammonia. *Appl. Catal. B Environ. Energy* **2024**, *351*, 123967. https://doi.org/10.1016/j.apcatb.2024.123967.

(94) Wang, G.; Chen, Q.; Zhang, J.; An, X.; Liu, Q.; Xie, L.; Yao, W.; Sun, X.; Kong, Q. Ru Doped NiMoO4 Nanoarray as a High-Efficiency Electrocatalyst for Nitrite Reduction to Ammonia. *J. Colloid Interface Sci.* **2024**, *661*, 401–408. https://doi.org/10.1016/j.jcis.2024.01.195.

(95) Wang, F.; Zhao, H.; Zhang, G.; Zhang, H.; Han, X.; Chu, K. Electroreduction of Nitrite to Ammonia Over Ni1Ru Single-Atom Alloys. *Adv. Funct. Mater.* **2024**, *34* (3), 2308072. https://doi.org/10.1002/adfm.202308072.

(96) Ren, Y.; Zhou, Q.; Li, J.; He, X.; Fan, X.; Fu, Y.; Fang, X.; Cai, Z.; Sun, S.; Hamdy, M. S.; Zhang, J.; Gong, F.; Liu, Y.; Sun, X. Ruthenium Doping: An Effective Strategy for Boosting Nitrite Electroreduction to Ammonia over Titanium Dioxide Nanoribbon Array. *J. Colloid Interface Sci.* **2023**, *645*, 806–812. https://doi.org/10.1016/j.jcis.2023.05.020.

(97) Ji, X.; Ma, C.; Zhang, F.; He, X.; Fan, X.; Li, J.; Li, Z.; Ouyang, L.; Zhang, L.; Li, T.; Zhao, D.; Wang, Y.; Zhang, J.; Cai, Z.; Sun, S.; Alshehri, A. A.; Lu, Q.; Sun, X. Ni@TiO2 Nanoarray with the Schottky Junction for the Highly Selective Electrochemical Reduction of Nitrite to Ammonia. *ACS Sustain. Chem. Eng.* **2023**, *11* (7), 2686–2691. https://doi.org/10.1021/acssuschemeng.2c06620.

(98) Cai, Z.; Ma, C.; Zhao, D.; Fan, X.; Li, R.; Zhang, L.; Li, J.; He, X.; Luo, Y.; Zheng, D.; Wang, Y.; Ying, B.; Sun, S.; Xu, J.; Lu, Q.; Sun, X. Ni Doping Enabled Improvement in Electrocatalytic Nitrite-to-Ammonia Conversion over TiO2 Nanoribbon. *Mater. Today Energy* **2023**, *31*, 101220. https://doi.org/10.1016/j.mtener.2022.101220.

(99) Li, Y.; He, X.; Chen, J.; Fan, X.; Yao, Y.; Ouyang, L.; Luo, Y.; Liu, Q.; Sun, S.; Cai, Z.; Alfaifi, S.; Du, J.; Zheng, B.; Sun, X. 3D Cauliflower-like Ni Foam: A High-Efficiency Electrocatalyst for Ammonia Production via Nitrite Reduction. *Chem. Commun.* **2023**, *59* (72), 10805–10808. https://doi.org/10.1039/d3cc03121g.

(100) Yang, L.; Wang, C.; Li, Y.; Ge, W.; Tang, L.; Shen, J.; Zhu, Y.; Li, C. Frustrated Lewis Pairs on Zr Single Atoms Supported N-Doped TiO2-x Catalysts for Electrochemical Nitrate Reduction To Ammonia. *Adv. Funct. Mater.* **2024**, *34* (36), 2401094. https://doi.org/10.1002/adfm.202401094.

(101) Du, H.; Guo, H.; Wang, K.; Du, X.; Beshiwork, B. A.; Sun, S.; Luo, Y.; Liu, Q.; Li, T.; Sun, X. Durable Electrocatalytic Reduction of Nitrate to Ammonia over Defective Pseudobrookite Fe2TiO5 Nanofibers with Abundant Oxygen Vacancies. *Angew. Chemie* **2023**, *135* (5), e202215782. https://doi.org/10.1002/ange.202215782.

(102) Fan, X.; He, X.; Ji, X.; Zhang, L.; Li, J.; Hu, L.; Li, X.; Sun, S.; Zheng, D.; Luo, Y.; Wang, Y.; Xie, L.; Liu, Q.; Ying, B.; Sun, X. High-Efficiency Electrosynthesis of Ammonia with Selective Reduction of Nitrite over an Ag Nanoparticle-Decorated TiO2 Nanoribbon Array. *Inorg. Chem. Front.* **2023**, *10* (5), 1431–1435. https://doi.org/10.1039/d2qi02409h.

(103) Wang, H.; Zhang, F.; Jin, M.; Zhao, D.; Fan, X.; Li, Z.; Luo, Y.; Zheng, D.; Li, T.; Wang, Y.; Ying, B.; Sun, S.; Liu, Q.; Liu, X.; Sun, X. V-Doped TiO2 Nanobelt Array for High-Efficiency Electrocatalytic Nitrite Reduction to Ammonia. *Mater. Today Phys.* **2023**, *30*, 100944. https://doi.org/10.1016/j.mtphys.2022.100944.

(104) Guo, Y.; Zhang, R.; Zhang, S.; Zhao, Y.; Yang, Q.; Huang, Z.; Dong, B.; Zhi, C. Pd Doping-Weakened Intermediate Adsorption to Promote Electrocatalytic Nitrate Reduction on TiO2 Nanoarrays for Ammonia Production and Energy Supply with Zinc-Nitrate Batteries. *Energy Environ. Sci.* **2021**, *14* (7), 3938–3944. https://doi.org/10.1039/d1ee00806d.

(105) Du, W.; Sun, Z.; Chen, K.; Wang, F.; Chu, K. Nb1-Zr Dual Active Sites Constructed on ZrO2 Boost Nitrite-to-Ammonia Electroreduction. *Chem. Eng. J.* **2024**, *481*, 148733. https://doi.org/10.1016/j.cej.2024.148733.

(106) Du, W.; Zhang, Y.; Chen, K.; Zhang, G.; Chu, K. Mo Single-Atom Catalyst Boosts Nitrite Electroreduction for Ammonia Synthesis. *J. Clean. Prod.* **2023**, *424*, 138875. https://doi.org/10.1016/j.jclepro.2023.138875.

(107) Zhang, Y.; Wan, Y.; Liu, X.; Chen, K.; Chu, K. Nb-Doped NiO Nanoflowers for Nitrite Electroreduction to Ammonia. *iScience* **2023**, *26* (10). https://doi.org/10.1016/j.isci.2023.107944.

(108) Liu, Q.; Wen, G.; Zhao, D.; Xie, L.; Sun, S.; Zhang, L.; Luo, Y.; Ali Alshehri, A.; Hamdy, M. S.; Kong, Q.; Sun, X. Nitrite Reduction over Ag Nanoarray Electrocatalyst for Ammonia Synthesis. *J. Colloid Interface Sci.* **2022**, *623*, 513–519. https://doi.org/10.1016/j.jcis.2022.04.173.